JOURNAL OF TISSUE ENGINEERING AND REGENERATIVE MEDICINE
J Tissue Eng Regen Med 2017.
DOI: 10.1002/term.2374

RESEARCH ARTICLE

Skin regeneration with all accessory organs following ablation with irreversible electroporation

Alexander Golberg[1,2*], Martin Villiger[3], G. Felix Broelsch[4], Kyle P. Quinn[5,6], Hassan Albadawi[7†], Saiqa Khan[4], Michael T. Watkins[7], Irene Georgakoudi[5], William G. Austen Jr[4], Marianna Bei[1], Brett E. Bouma[3,8], Martin C. Mihm Jr[9] and Martin L. Yarmush[1,10*]

[1]*Center for Engineering in Medicine, Department of Surgery, Massachusetts General Hospital, Harvard Medical School, and the Shriners Burns Hospital, Boston, MA, 02114, USA*
[2]*Porter School of Environmental Studies, Tel Aviv University, Tel Aviv, Israel*
[3]*Wellman Center for Photomedicine and Department of Dermatology, Massachusetts General Hospital and Harvard Medical School, 50 Blossom Street, Boston, Massachusetts, 02114, USA*
[4]*Department of Surgery, Division of Plastic and Reconstructive Surgery, Massachusetts General Hospital, Harvard Medical School, Boston, MA, 02114, USA*
[5]*Department of Biomedical Engineering, Tufts University, Medford, MA, 02155, USA*
[6]*Department of Biomedical Engineering, University of Arkansas, Fayetteville, AR, 72701, USA*
[7]*Division of Vascular and Endovascular Surgery, Massachusetts General Hospital, Harvard Medical School, Boston, MA, 02114, USA*
[8]*Harvard-Massachusetts Institute of Technology Division of Health Sciences and Technology, Cambridge, Massachusetts, 02142, USA*
[9]*Department of Dermatology, Brigham and Women's Hospital, Harvard Medical School, Boston, MA, 02115, USA*
[10]*Department of Biomedical Engineering, Rutgers University, Piscataway, NJ, 08854, USA*

Abstract

Skin scar formation is a complex process that results in the formation of dense extracellular matrix (ECM) without normal skin appendages such as hair and glands. The absence of a scarless healing model in adult mammals prevents the development of successful therapies. We show that irreversible electroporation of skin drives its regeneration with all accessory organs in normal adult rats. Pulsed electric fields at 500 V, with 70 µs pulse duration and 1000 pulses delivered at 3 Hz, applied through two electrodes separated by 2 mm lead to massive cell death. However, the ECM architecture of the skin was preserved. Six months after the ablation, the epidermis, sebaceous glands, panniculus carnosus, hair follicles, microvasculature and arrector pili muscle were altogether re-formed in the entire ablated area. These results suggest a key role of the ECM architecture in the differentiation, migration and signalling of cells during scarless wound healing. Copyright © 2016 John Wiley & Sons, Ltd.

Received 23 February 2016; Revised 12 November 2016; Accepted 6 December 2016

Keywords **scar; skin; regeneration; scarless; pulsed electric field; electroporation; extracellular matrix**

1. Introduction

Scars, caused by trauma or burn injury, remain an enigma throughout the long history of human medicine. Scar formation is a complex process involving the interplay of growth factors, proteolytic enzymes, angiogenesis factors and fibrogenic factors, which stimulate the increased deposition of extracellular matrix (ECM) by myofibroblasts (Duffield *et al.*, 2013). Numerous studies have identified genomic (Smith *et al.*, 2008; Thompson *et al.*, 2013), epigenetic (Gibran, 2014; Russell *et al.*, 2010) and environmental factors (Eto *et al.*, 2012) that favour the formation of scars; however, the exact mechanisms inducing the formation of scar tissue rather than normal skin are unknown (Duffield *et al.*, 2013). Current data show that alterations in coagulation, inflammation, angiogenesis, fibroplasia, contraction, remodelling (DiPietro, 2013; Koh and DiPietro, 2011; Robson, 2003) and mechanical tension correlate with an increased proliferation of scars (Aarabi *et al.*, 2007; Seifert *et al.*, 2012; Wong *et al.*, 2011). But, as of yet, the role of the ECM and corresponding molecular mechanisms that induce scarring are not well understood, due to the lack of scarless regeneration in mammals. This gap of knowledge limits our fundamental understanding of tissue remodelling and leads to limited clinical success of the treatment of scars (Sonnemann and Bement, 2011). Interestingly, recent studies reported decreased fibrosis in the liver tissue following tumour ablation in humans using irreversible electroporation (IRE); (Narayanan, 2011).

Irreversible electroporation is a non-thermal tissue ablation technique, where pulsed electric fields cause irreversible damage to cells by creating nanoscale pores in the cellular membrane, while sparing the surrounding tissue scaffold, large blood vessels and other accessory

---

*Correspondence to: Alexander Golberg, Porter School of Environmental Studies, Tel Aviv University, Tel Aviv, Israel. Martin L. Yarmush, Center for Engineering in Medicine, Department of Surgery, Massachusetts General Hospital, Harvard Medical School, and the Shriners Burns Hospital, Boston, MA, 02114, USA. E-mail: agolberg@tauex.tau.ac.il

[†] Present address: Interventional Radiology Research Laboratory, Mayo Clinic, Scottsdale, AZ 85259, USA.

structures (Golberg and Yarmush, 2013; Phillips *et al.*, 2010; Rubinsky *et al.*, 2007; Sano *et al.*, 2010). Several hypotheses describing the mechanisms of IRE-associated cell death have been proposed, including deformation of the cellular membrane lipid layer (Crowley, 1973; Michael and O'Neill, 1970; Steinchen *et al.*, 1982), altered phase transition (Sugár, 1979), breakdown of interfaces between the lipid domains with different compositions (Cruzeiro-Hansson and Mouritsen, 1988), or denaturing of the membrane proteins (Tsong, 1991). However, all these explanations remain inconclusive (Weaver and Chizmadzhev, 1996). Recently, investigators proposed that IRE induces aqueous pores in the lipid bilayer (Kotnik *et al.*, 2012; Spugnini *et al.*, 2007; Weaver and Chizmadzhev, 1996), largely based on thermodynamic rationales, as the aqueous pores start by penetration of water molecules into the lipid bilayer when the applied pulsed electric field transmembrane potential threshold is achieved (Kotnik *et al.*, 2012). This leads to reorientation of the adjacent lipids with their polar head groups facing the water molecules forming stable pores (Kotnik *et al.*, 2012). When the IRE field creates large enough and constant pores, this could subsequently lead to cell death. IRE has been used in multiple clinical trials to ablate solid tumours (Chunlan *et al.*, 2015), and to treat cardiac arrhythmias (Deodhar *et al.*, 2011). Previous studies suggest that IRE causes cell death while preserving the ECM as well as the vasculature, and leads to tissue regeneration (Rubinsky *et al.*, 2007).

Our previous work has shown that mild pulsed electric fields lead to skin injury resulting in rejuvenation (Golberg *et al.*, 2015b). Furthermore, we have recently shown that completely ablated normal rat liver regenerates without fibrosis (Golberg *et al.*, 2016a), confirming the earlier hypothesis (Rubinsky *et al.*, 2007). In addition, we have also shown that partial IRE reduces scars after burn injury in rats (Golberg *et al.*, 2016b). The importance of the ECM for functional tissue regeneration has long been recognized, and multiple attempts of tissue engineering aspire to re-engineer the matrix architecture (Place *et al.*, 2009). However, the importance of naïve ECM organization in the wound healing has not been demonstrated *in vivo*, because of the lack of a suitable model. Based on these findings, we tested the hypothesis whether calibrated IRE treatment causes skin ablation associated with preservation of tissue ECM and scarless tissue regeneration in rats.

2. Materials and methods

2.1. Animals

Female Sprague–Dawley rats (~200 g, $N = 104$, 6 weeks old) were purchased in Charles River Laboratories (Wilmington, MA, USA). The animals were housed in cages with access to food and water *ad libitum*, and were maintained on a 12-h light/dark cycle in a temperature-controlled room. All animal procedures were approved by the Institutional Animal Care and Use Committee (IACUC) of the Massachusetts General Hospital. All procedures were in accordance with the guidelines of the National Research Council.

2.2. Irreversible electroporation

Prior to IRE treatment, animals ($N = 5$ per each time point) were anaesthetized with isoflurane. Their fur was clipped along the dorsal surfaces and treated with depilatory cream (Sally Hansen®Div. Del Laboratories, Farmingdale, NY, USA). Subsequently, a designated area was subjected to electroporation using contact electrodes with a surface area of 1 cm^2. Pulsed electric fields (PEF) specifications are as follows: 1000 pulses, 500 V, 2 mm gap between the electrodes, 70 μs duration, 3 Hz. Square pulses were delivered using a BTX 830 pulse generator (Harvard Apparatus, Holliston, MA, USA). Currents were measured *in vivo* using a PicoScope 4224 Oscilloscope with Pico Current Clamp (60A AC/DC) and analysed with Pico Scope 6 software (Pico Technologies, UK).

2.3. Numerical modelling of the electric field distribution

The electrical and thermal properties of the skin layers used for the modelling (QuickField Software, Terra Analysis, Denmark) appear in Table S1 (Hasgall *et al.*, 2014; Pavšelj and Miklavčič, 2008). Skin tissue features both electrical properties: resistance and capacitance. However, the charging time of the capacitive component of healthy skin is very small (~1 μs) in comparison to the pulse duration used in this study (70 μs; Weaver, 2000). Thus, we used a direct current conductance model to calculate the distribution of the electric field in the heterogeneous skin. To estimate the local electric field strength at each point in the skin, we used the Laplace equation as follows:

$$\frac{\partial}{\partial x}\left(\sigma_x(E)\cdot\frac{\partial U}{\partial x}\right)+\frac{\partial}{\partial y}\left(\sigma_y(E)\cdot\frac{\partial U}{\partial y}\right)=0 \qquad (1)$$

where σ is the electrical conductivity (Siemens/m1), and U (Volts) is the electric potential. We calculated the electric field distribution in the different skin layers under the following boundary conditions applied on the two electrodes: cathode 0 V and anode 500 V. The thermal model for the similar electroporation setup was developed previously (Golberg *et al.*, 2015b).

2.4. Burn injury

Before the creation of third-degree burns, the animals ($N = 5$ per each time point) were anaesthetized with isoflurane and their fur was clipped along the dorsal surfaces. Burns were incurred by pressing the end of a pre-heated (≥ 95°C) brass block against the rat's dorsum for 10 s, resulting in a non-lethal, full-thickness, third-degree burn, measuring approximately 1 cm^2. Burn injury

DOI: 10.1002/term

and IRE were performed on the same animals on sites 2 cm apart from each other along the head to tail axis.

2.5. Polarization-sensitive optical coherence tomography

Polarization-sensitive optical coherence tomography (PS-OCT) was performed as reported in detail previously (Lo *et al.*, 2016; Villiger *et al.*, 2013). In short, a wavelength-swept laser source operating at a centre wavelength of 1320 nm was used, achieving an axial resolution of 9.4 μ m and operating at an A-line rate of 54 kHz. Volumetric imaging was performed by scanning an area of 10 × 5 mm, consisting of 2048 A-lines/image × 256 images, with a focused beam featuring a lateral resolution of 15 μm. The lesions were apposed against a glass slide with ultrasound-gel as immersion liquid to centre the superficial layers in focus. Two–three volumes were acquired for each lesion and time point, overlapping the fields of view to image the entire lesions. The polarization state of the input light was modulated between circular and linear polarization between adjacent A-lines, and the signal was detected with a polarization diverse receiver. Longitudinal imaging was performed on three animals at 0, 6, 12, 24 and 72 h, and 1, 2, 3, 4, 5, 8, 12, 16, 20 and 24 weeks.

The data were reconstructed with spectral binning (Villiger *et al.*, 2013), using $1/5^{th}$ of the spectral bandwidth, a lateral Gaussian filter with a full-width at half-maximum equal to 12 adjacent A-lines, and an axial offset of 48 μm to derive tissue birefringence. Tissue birefringence rotates the polarization state of the probing light, as visualized on the Poincaree-sphere, and is expressed in deg/μm. The degree of polarization (DOP) was evaluated independently for each spectral bin and input polarization state over the same lateral Gaussian kernel, and then averaged. DOP expresses the randomness of the measured polarization states in small neighbourhood and scales from 0 (completely random) to unity (uniform). The structural intensity tomograms are displayed in logarithmic scale as grey-scale images. Birefringence was mapped from 0 to 1.2 deg/μm with an isoluminant colour-map, and overlayed with the grey-scale intensity image. DOP is scaled from 0.5 to 1, and is rendered in the same colour-map. For quantitative analysis, the various time points were aligned, and the mean birefringence and DOP over the identical central cylindrical region of diameter 1.4 mm and 0.25 mm height, centred 0.5 mm below the tissue surface, were computed. The errors were computed over the same region.

2.6. Laser Doppler scanning

A laser Doppler imager (Moor Instruments, Wilmington, DE, USA) was used to assess blood flow. The laser Doppler source was mounted on a movable rack exactly 10 cm above the dorsum of the rat after the animal was anaesthetized and restrained on the underlying table. Five animals were imaged at each time point. The laser beam (780 nm) reflected from circulating red blood cells in capillaries, arterioles and venules was detected and processed to provide a computerized, colour-coded image. By using image analysis software (Laser Doppler Perfusion Measure, Version 3.08; Moor Instruments), mean flux values representing blood flow were calculated from the relative flux units for the areas corresponding to the dorsum of the rats. The analysed region of interest was 0.25 by 0.25 cm. Baseline images were obtained from each rat before treatment was administered. Then, the rats were treated by IRE or burn, and serial laser Doppler images were obtained subsequently. For analysis, we calculated the ratio of the mean flux value at the centre of the treated area (black box, Figure 7q) with the mean flux value at the edge of the treated area (white box, Figure 7q).

2.7. Skin mechanical properties measurement

To assess skin mechanical properties, we performed tensile mechanical testing on excised samples. Skin at the treated sites (1 cm^2) was excised at 1 day, 3 days, 1 week, 3 weeks, 2 months and 6 months (five animals per time point). Skin samples were placed in standard saline solution before tension measurement. Tension measurements were performed within 1 h after the excision. Before measurement, the thickness of each sample was measured. Skin samples were mounted on the Expert4000 tensiometer (ADMET, MA, USA). The load was applied using a 1000 g-Tension-1344004 transducer. 'Stress at extension'-type of analysis was chosen on the MTESTQuattro software (ADMET, MA, USA). Stress was applied using a ramp waveform to cause a 2 mm/min extension rate. The elongation/stress data were exported to Microsoft Excel ver.7. Young's modulus was extracted from the linear part of the stress–strain curve using the following equation 2:

$$Y = \frac{F/A_0}{\Delta L/L_0} \tag{2}$$

where Y (N/mm^2) is the elastic Young's modulus, F *(N)* is the applied force, A_0 is the cross-section of the skin samples, ΔL (mm) is the elongation of the skin sample under force, and L_0 (mm) is the original length of the tested sample.

2.8. Histology

Specimens were harvested immediately after the injury, 6 h, 12 h, 1 day, 3 days, 1 week, 3 weeks, 2 and 6 months following the initial treatment. Five animals were killed for each time point. Five animals were used as controls. Skin samples were fixed in 10% formalin, embedded in paraffin, and cut into 7-μm-thick sections. Sections were stained with haematoxylin and eosin (H&E), Herovici, Masson's trichrome and Verhoeff–Van Gieson stain. Tissues were processed and stained by the Rodent

Histopathology Core at Harvard Medical School. Slides were evaluated by three individual investigators, including an experienced dermatopathologist. Two investigators were blinded to the origin of the specimens. Colour images of each entire tissue section were acquired using a NanoZoomer Digital Pathology System (Nanozoomer 2.0-HT slide scanner, Hamamatsu, Hamamatsu City, Japan).

2.9. Automated image analysis of trichrome stain for fibre density and orientation

Fibre density and orientation were calculated from images of Masson's Trichrome-stained sections using previously established image processing algorithms (Quinn *et al.*, 2015). Briefly, collagen fibres were identified from the images (five animals at each time point) where the ratio of blue-to-red intensities exceeded a value of 2. Local fibre density was determined by the relative amount of collagen-positive pixels within a 90 pixel radius. Fibre orientation surrounding each image pixel location was also computed, and directional statistics were employed to compute the local directional variance of the fibres within a 50 pixel radius. Directional variance provided a metric that was inversely proportional to the strength of fibre alignment in a preferred direction. Subregions of 300 × 700 μm corresponding to the centre of the PEF-treated tissue region were defined through blinded evaluation of the original Trichrome images, and the average fibre density and directional variance were computed from each subregion.

2.10. Quantification of morphological markers

To quantify the effects of IRE and burns, we quantified (five for each treatment and each experimental point) the whole skin thickness, stratum coreum thickness, epidermis thickness, dermis thickness, fat layer thickness and muscle layer thickness at least at 25 locations and five sections obtained from different animals killed at the same time point. The number of viable hair follicles, sebaceous glands and arrector pili muscles, and viable nerves was counted per 2 mm of line parallel with the epidermis. Fibroblasts were counted in five fields of view (150 × 500 μm) on each section. The total number of mast cells, stained with Toloiden, was counted in three fields of view (20 × magnification) per slide.

2.11. Immunohistochemistry of rat skin tissue

Eight-micrometere-thick paraffin-embedded tissue sections on glass slides were baked at 56°C for 30 min followed by deparaffinization in xylene and rehydration in graded alcohol into water. Antigen retrieval was performed by boiling the slides in 10 mM sodium citrate buffer pH 6.0 for 30 min. Tissue sections (five animals for each treatment and each experimental time point) were permeabilized with 0.1% Triton X-100. Endogenous peroxidase activity was quenched with 3% hydrogen peroxide in 60% methanol for 30 min. Biotin activity was blocked with Avidin-Biotin blocking reagent kit (Life Technologies, Grand Island, NY 004303, USA). Non-specific proteins were blocked with 5% animal serum corresponding to the host species of the secondary antibodies. Tissue sections were incubated overnight with mouse monoclonal antibodies diluted in 5% horse serum that recognize the following proteins; p63 (Biocare, CM163A, 1:200), Nestin (AbCam #6142, Cambridge, MA, USA, 1:200) and BMP-4 (Santa Cruz Biotechnology, Santa Cruz, CA, USA, SC-393329, 1:100), followed by 60 min incubation with horse-anti mouse biotinylated secondary IgG diluted 1:300 (Vector Laboratories). The following rabbit polyclonal antibodies were diluted in 5% goat serum and used to recognize the following proteins; Nephronectin (Abcam #64419, Cambridge, MA, USA, 1:100), Laminin (Abcam #11575, Cambridge, MA, USA, 1:200), followed by incubation with goat anti-rabbit peroxidase-conjugated IgG (Cell Signaling #7074, 1:200). After washing, slides were incubated with biotinylated secondary IgG at 1:300 dilutions (Vector Laboratories) for 60 min at room temperature followed by incubation with avidin/biotinylated enzyme complex reagent (ABC kit, Vector Laboratories PK6100) for 30 min. The following goat polyclonal antibodies were diluted in 5% horse serum and used to recognize FGF-5 (Santa Cruz Biotechnology, SC-1363, 1:100) or LEF-1 (Santa Cruz Bitechnology, SC-8591, 1:100). Finally, rabbit polyclonal antibodies diluted in 5% goat serum were used to recognize Cytokeratin-17 (Santa Cruz Biotechnology, SC-101931, 1:100) or Collagen-IV (Abcam, 6586, 1:50). The relevant slides were incubated with either horse anti-goat or goat anti-rabbit peroxidase-conjugated secondary IgGs (Vector Laboratories, Burlingame, CA, USA, 1:200) for 60 min at room temperature. Specific proteins were visualized by reacting the slides with 3,3′-diaminobenzidine substrate in the presence of hydrogen peroxide in a reaction buffer (Vector Laboratories SK4100). Tissue sections were briefly counterstained with Gill-haematoxylin. Slides were briefly dehydrated and then mounted with Histomount solution (Life Technology, Grand Island, NY 008030, USA). Colour images of each entire tissue section were acquired using NanoZoomer Digital Pathology System (Nanozoomer 2.0-HT slide scanner, Hamamatsu, Hamamatsu City, Japan).

2.12. TUNEL apoptosis assay

Eight-micrometre-thick paraffin-embedded tissue sections on glass slides were baked at 56°C for 30 min followed by deparaffinization in xylene and rehydration from graded alcohol into water. Antigen retrieval was performed by incubating the slides in a microwave oven at 752 W for 5 min in 100 mM sodium citrate buffer pH 3.0. Then the slides were washed in phosphate-buffered saline (PBS) for 15 min. Additional treatment in microwave at 752 W for 5 min in 100 mM sodium citrate buffer pH 3.0 and rinse in PBS. Next, the slides were treated with proteinase K (Sigma, IS, 20 μg/mL) for 15 min at room temperature. The non-specific proteins were blocked by incubation in 20% normal bovine serum for 30 min at RT. The slides were washed three times in PBS for 3 min. TUNEL assay reagents (Molecular Probes, CA, USA) were prepared and the assay was used according to manufacturer's protocol.

2.13. Transmission electron microscopy

Tissues were fixed in 2.0% glutaraldehyde in 0.1 M sodium cacodylate buffer, pH 7.4 (Electron Microscopy Sciences, Hatfield, PA, USA) overnight at 4°C. They were rinsed in buffer, post-fixed in 1.0% osmium tetroxide in cacodylate buffer for 1 h at room temperature, rinsed in buffer again, and dehydrated through a graded series of ethanol to 100%, followed by 100% propylene oxide. They were then infiltrated with Epon resin (Ted Pella, Redding, CA) in a 1:1 solution of Epon:propylene oxide overnight at RT on a rocker. The following day they were placed in fresh Epon for several hours and then embedded in Epon overnight at 60°C. Thin sections (70–80 nm) were cut on a Leica EM UC7 ultramicrotome, collected onto formvar-coated grids, stained with uranyl acetate and lead citrate, and examined in a JEOL JEM 1011 transmission electron microscope at 80 kV. Images were collected using an AMT digital imaging system (Advanced Microscopy Techniques, Danvers, MA).

2.14. Cytokines/chemokine/growth factor determination

Tissue was harvested at 6 h, 2 and 5 weeks after injury (three animals per injury and time point), immediately flash frozen in liquid nitrogen and kept at −80 °C. In this study, only one type of injury was done for each animal, to avoid paracrine effects. The centre of the IRE-treated area was excised and proteins were extracted in CelLytic™ MT Cell Lysis Reagent, C3228 (Sigma, MO) mixed with Protease Inhibitor Cocktail P8340 (Sigma, MO), which was homogenized using Mini-Beadbeater-1 (Biospec, OK) with 5.5 g/cc density zirconia beads (Biospec, OK). Tubes with the buffer and beads were shaken four times for 15 s at 1-min intervals, and then the tubes were kept on ice. Immediately after the extraction, total protein was quantified using 660 nm Protein Assay reagent (Pierce, IL). All samples were then diluted to a single concentration; quantification of cytokines, chemokines and growth factors was performed using MILLIPLEX MAP Rat Cytokine/Chemokine Magnetic Bead Panel and TGF-beta 3-Plex Array (Eve Technologies, Calgary, AB, Canada). After quantification, the concentration of each factor was normalized to the total protein concentration of each sample.

2.15. Statistical analysis

Statistical analysis was performed with the statistics toolbox of MATLAB, R2009b (MathWorks, Natick, MA). For all values besides cytokine analysis, data reported are means ± STD of the mean. Statistical analysis was performed by use of the unpaired, one-tailed, *t*-test if not stated otherwise. Significance was set at $P < 0.05$. In the cytokine analysis assays, the correction for the *P*-value was made assuming 26 independent events, and thus the significance in the expression differences was set for $P < 0.002$; data reported are means ± STD.

3. Results and discussion

To assess the effects of IRE on normal skin ablation and the subsequent regeneration process, we ablated an area of 1 cm^2 of shaved dorsal skin of female Sprague–Dawley rats with pulsed electric fields (Figure 1a). Full-thickness third-degree thermal burns that typically lead to scar formation and prevent accessory organ regeneration were used to compare the outcome of IRE treatment. The following IRE treatment parameters were used to minimize the thermal effects of pulsed electric fields on tissue: applied voltage (E) 500 V, 2 mm gap between electrodes, pulse duration (t_p) 70 μs, pulse delivery frequency (f) 3 Hz, total number of pulses (N) 1000, delivered in groups of 100 with 1 s interval between groups. Notably, this IRE dose is an order of magnitude larger than the doses currently used for the ablation of solid tumours (Philips *et al.*, 2013). The experimentally measured current (Figure 1b) revealed a continuously increasing current with increasing pulse number, indicating a successful membrane electroporation effect (Ivorra *et al.*, 2009).

Depending on the strength of the local electric field, pulsed electric fields can lead to IRE or reversible electroporation of the membrane, or can have no effect (Yarmush *et al.*, 2014). IRE is achieved when the transmembrane potential exceeds a certain threshold value (Yarmush *et al.*, 2014). To understand the effects of pulsed electric fields on cells in the skin, it is necessary to estimate the electric field distribution throughout the complex tissue structure. This can be challenging, as the skin is a heterogeneous organ, composed of multiple compartments with distinct electric conductivities (Pavšelj and Miklavčič, 2008). To this end, we generated a finite element model, modelling the skin as discrete layers (Figure 1c). The numerical simulation reveals a reduction of the electric field strength in the layers of skin closest to the electrodes (stratum corneum, epidermis and dermis; Figure 1d). An additional drop occurs in the panniculus carnosus. The strongest electric field develops in the subcutaneous tissue layer, which can be exposed to a field strengths that is fourfold higher than the epidermis and dermis areas and fivefold higher than the panniculus carnosus.

DOI: 10.1002/term

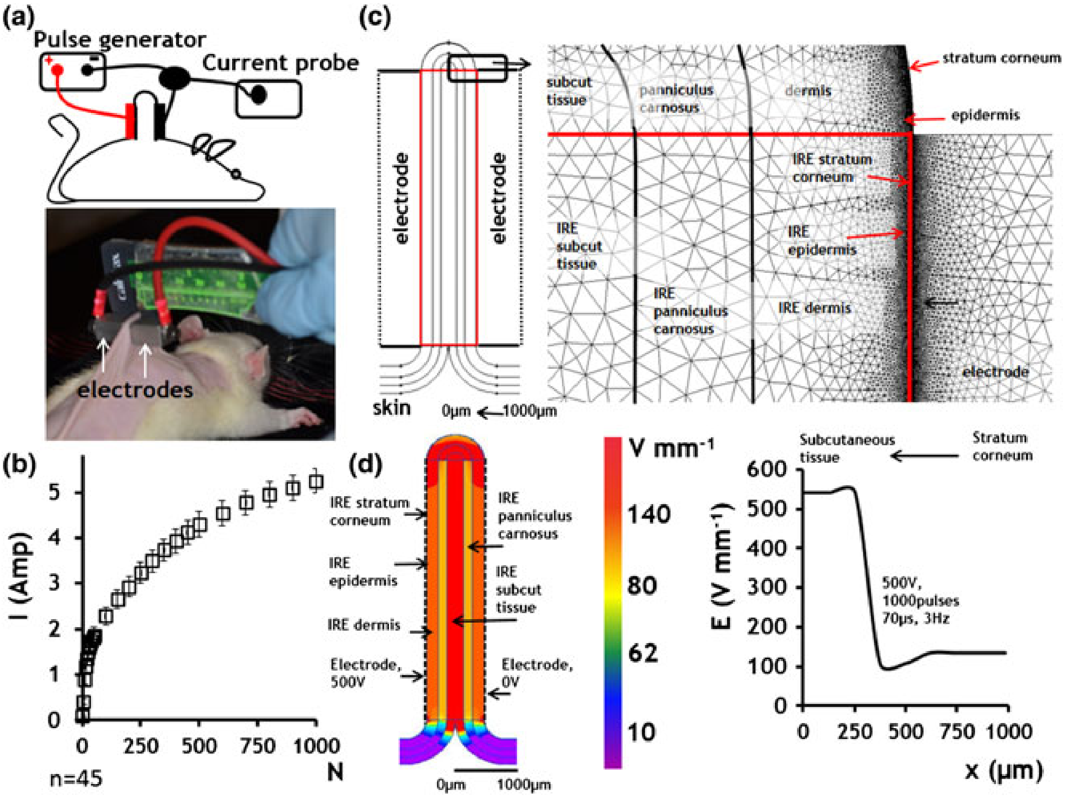

Figure 1. Irreversible electroporation (IRE) procedure. (a) Electrode positioning. (b) Current measured during pulse delivery) $n = 45$). (c) Geometry and mesh of the finite element numerical model of rat skin, with all major composing layers. The skin is divided into two regions: (1) control skin (CS); and (2) IRE-ablated skin (IRES). IRES layers are tagged with IRE sign. (d) Electric field distribution in different skin layers under various boundary conditions. The panel on the left shows the 2D map of electric field distribution. The plot on the right shows the numerical values of the electric field strength in different skin layers [Colour figure can be viewed at wileyonlinelibrary.com]

To investigate the temporal evolution of cutaneous injury and regeneration of skin structure following IRE treatment in rats, we longitudinally imaged individual lesions at multiple time points *in vivo* with PS-OCT (Lo *et al.*, 2016; Villiger *et al.*, 2013). We have recently established the methodology for PS-OCT imaging of hypertrophic scars in a rat model (Lo *et al.*, 2016). In addition to providing structural information, PS-OCT also measures the polarization properties of the sample. By analysing how the polarization state of the scattered light changes as a function of depth, a measure of tissue birefringence can be obtained. Regularly arranged collagen fibres are the most prominent source of birefringence in tissue detected by PS-OCT. The collagen fibre thickness and density correlate with higher birefringence values. In contrast, if collagen fibres are present, albeit arranged irregularly on a size-scale smaller or comparable to the focal volume of OCT (10 × 15 μm), then the measured polarization states change randomly between adjacent pixels, which manifests as a reduction of the DOP. This is the case for the intercalated arrangement of collagen fibres in normal skin, resulting in a rapid decrease of the DOP and an irregular appearance of birefringence values. Together, these polarization parameters provide important cues on collagen organization, quantity and morphology.

For histological assessment, we harvested samples immediately ($T = 0$), or at 6 h, 12 h, 24 h, 3 days, 1 week, 3 weeks, 8 weeks or 24 weeks after the IRE and burn injuries. IRE-ablated skin (IRES) appeared blanched immediately after the injury. In the samples harvested immediately after the injury, histological observations showed marked thinning of the dermis and panniculus carnosus with evident diffused necrosis of the epidermis with marked parakeratosis (Figure S1a). Superficial sebaceous glands also showed degenerative necrosis (Figure S1a). Superficial vessels all showed compaction of red blood cells and focal pignosis of endothelial cells (Figure S1a, insert, arrows). There were dilated lymphatics towards the deeper portion of the specimen and in the subcutanous tissue (Figure S1a, yellow arrow). Mast cell degranulation was observed in the muscle and lower dermis muscle and subcutaneous fascia (Figure S1a, insert). Multiple skeletal muscle fibres showed scattered more centralized nuclear localization, unlike the normal peripheral localization (Figure S1a, arrow). Six hours after ablation, the epidermis in the IRES was completely necrotic with extensive ulceration without visible intraepidermal abscesses (Figure S2). The hair follicles showed extensive destruction with marked pignosis of various layers. Subcutaneous fat and the dermis appeared collapsed. Panniculos carnosus muscle showed areas of complete loss of striation and fragmentation of fibres. The initiation of infiltration of neutrophils and leucocytes was observed. The dermal vessels in the upper half of the dermis showed compaction and red blood cell plugging (Figure S2). The vessels in the lower dermis also showed compaction, but mostly had empty lumen with clear signs of degeneration of red blood cells. The nerves showed swollen Swan cells (Figure S2, insert arrow).

Massive cell apoptosis in all skin layers was detected at 6, 12 and 24 h after IRE (Figure S3b–d). Twelve hours after ablation (Figure 2a), multifocal areas of inflammatory cell infiltration of the necrotic epidermis as well as in the superficial papillary dermis were observed. We found subcorneal abscess formation in the papillary dermis associated with neutrophil accumulation. The epidermis and the superficial external root sheath of hair follicles were all necrotic. The papillary dermis and reticular dermis showed oedema and all small venous were congested. Severe oedema was also observed in the subcutaneous fat, nerves and the muscle, where the muscles appeared separated. The vessels showed thrombus formation with little neutrophil infiltration. The muscle fibres showed an intense infiltration of neutrophils and were associated with focal loss of striation. Twenty-four hours after ablation, the epidermis showed complete necrosis (Figure 2b). The hair follicles and sebaceous glands in the ablated areas were completely necrotic. There were multiple neutrophils scattered throughout the dermis. Many more vessels had denuded endothelium. By 12 h, severe oedema persisted in the dermis and in the muscle. Nerves looked swollen and degenerated in several locations with pyknotic nuclei of Schwann cells. Muscle fibres were fragmented, lost striation and were infiltrated with leukocytes (Figure 2b).

Three days after IRE, the ablated area was mostly necrotic (Figure 2c) with rare apoptotic cells (Figure S3e). The areas of IRE skin were very clearly demarcated in the dermis and epidermis from the less affected skin on either site (Figure 2c). Its basic fibrillar architecture in the IRES was still present. In contrast, in the burned skin the architecture was completely lost immediately after injury. Most of the IRES was acellular. However, a band of neutrophils and lymphocytes started to form and

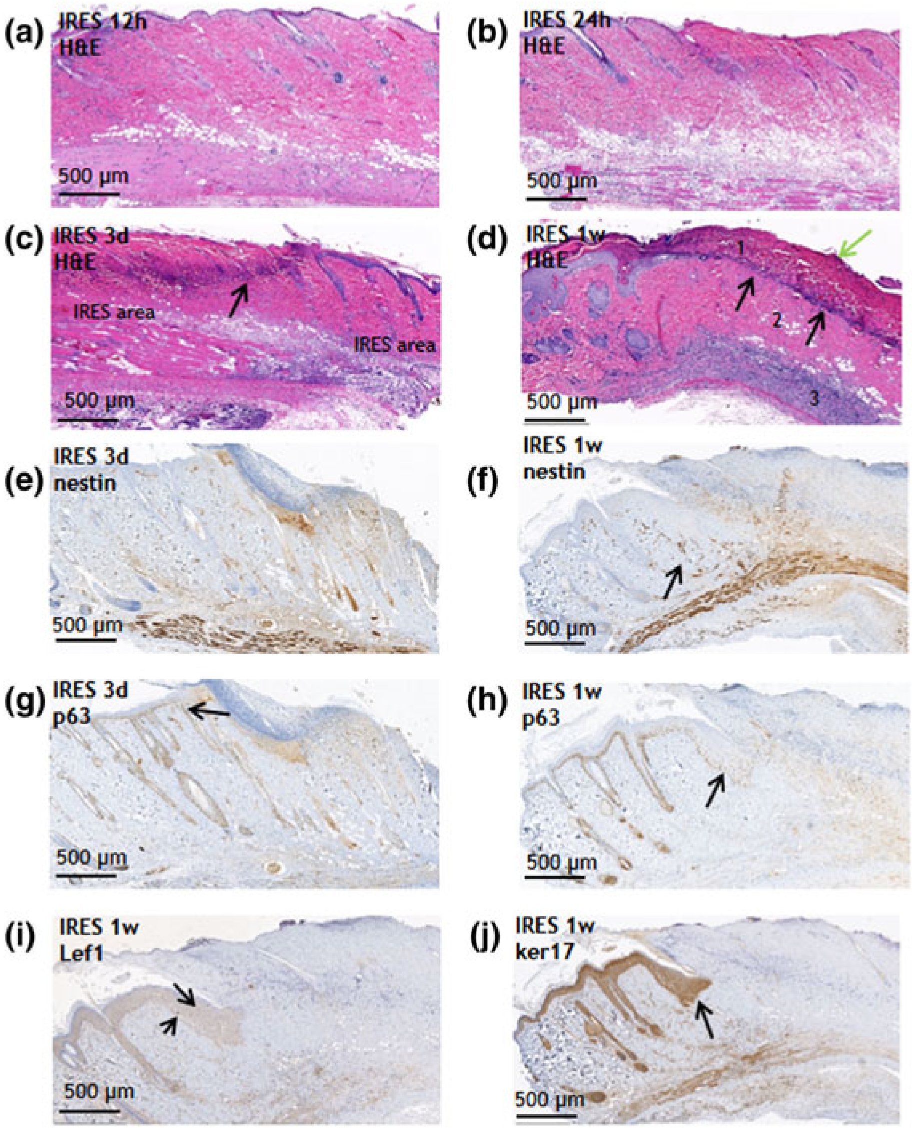

Figure 2. Early events post-irreversible electroporation (IRE) ablation of a normal rat skin. (a) 12 h post-IRE (H&E stain); (b) 24 h post-IRE (H&E stain); (c) 3 days post-IRE (H&E stain), arrow shows the neutrophils separation band; (d) 1 week post-IRE (H&E stain). Black arrow shows neutrophils separation band. Green arrow shows bacteria infection. Angiogenesis as detected with nestin at 3 days (e) and 1 week (f) after IRE. Activation and intrusion of the neighbouring epidermis to the injured side. Invading cells express p63 (g, h), Lef-1 (i) and ker17 (j). Arrows show cells that overexpress the indicated proteins [Colour figure can be viewed at wileyonlinelibrary.com]

separated affected dermis from less affected dermis (Figure 2c, arrow). The subcutaneous fat was not vital, but necrotic in all treated samples. Leftovers of hair follicles, completely necrotic, were observed. The nerves showed oedema and vascularization. Panniculus carnosus was necrotic. No significant angiogenesis at the periphery of the IRES area was detected 3 days after the ablation (Figure 2e). Massive accumulation of epithelial cells, strongly expressing p63, was detected on the periphery of the ablated area at 3 days after IRE (Figure 2g, arrow). At 1 week after the IRE, the ablation area was sharply demarcated (Figure 2d, numbers indicated the zones). The most superficial zone was covered by stratum corneum and showed eosinophylic material composed of multiple fibrils including ghost-like remnants of epidermis. Focally, there were bands of bacteria that formed aggregates in the eosinophilic-like epidermis (Figure 2d, green arrow). Scattered colonies of bacteria were present also in the eosinophilic dermal remnant. At the base of this superficial necrotic area there was a striking band resembling infiltrating neutrophils that completely separated the non-damaged, acellular dermis from the ghost-like infected dermis (Figure 2d, black arrows).

The second band was the zone of retention of normal collagen architecture but with swollen fibres and prominent hypocellularity. Few scattered fibroblasts and neutrophils were also observed. This zone incorporates the small portion of subcutaneous fat and area of marked degradation of muscle fibres that show some areas of calcification of fibres outlining the striations. No nerves, hair follicles or sebaceous glands were observed in the altered areas.

The third zone was the deep fascia with prominent cellularity comprised with fibroblasts and mast cells with apparent regeneration of collagen fibres and numerous scattered mast cells. In the area of the muscle the altered muscle cells were associated with moderate lymphocyte and neutrophil infiltration. There were signs of mitosis of the muscle cells. Massive angiogenesis was detected in the border between the viable and the ablated skin (Figure 2f, arrow indicates the formation of new small blood vessels as detected with nesting staining; Matsuda *et al.*, 2013). Epidermal growth was detected to be originating from the areas of viable skin localizing into the areas of ablated skin. The cells that originated from the area of the non-ablated skin were detected in the border zone of the growing epidermis and stained positive for p63, ker17 and Lef-1 (Figure 2h–j).

Our findings suggest that the early events following IRE treatment indicate an ongoing cellular loss that partially starts during the acute phase after treatment and may last for up to 1 week after ablation. Partial regeneration of certain skin layers, epidermis and panniculus carnosus start as early as 3 days after ablation. Because of continuous infiltration of inflammatory cells to the IRE-treated area, it is very difficult to assess cellular viability in the ablated area using markers of metabolic activity. The morphological assessments of samples obtained at 1, 3, 8 and 24 weeks after IRE are summarized in Table 1.

Preservation of the tissue architecture particularly sparing the ECM and large structures are major characteristics of IRE ablation as compared with other ablation methods (Golberg *et al.*, 2015a; Lee *et al.*, 2010; Rubinsky, 2007; Rubinsky *et al.*, 2007). However, very limited data are available on how this property affects scarless tissue regeneration (Golberg *et al.*, 2016a; Phillips *et al.*, 2010; Phillips *et al.*, 2012). In this study, we compared the skin structure following IRE with the skin structure after third-degree burn, which is known to destroy tissue architecture. In contrast to the burn injury, IRE did not change the ECM architecture as detected immediately after the ablation by both *in vivo* PS-OCT and histopathological analysis (Figures 3, S1 and S4). Histological sections of samples harvested immediately after the injury showed a 27% thinning of the IRES sample in comparison with untreated control skin (CS); burned skin (BS) thickness was unchanged in comparison with CS (Table 1). The stratum corneum was preserved in the IRES (Figures 3f and S1a), but was destroyed in the BS (Figures 3k and S1c). The epidermis cells were necrotic in both IRES and BS (Figures 3f,k and S1a,c). The dermal collagen showed a normal, reticular, intercalated structure of collagen fibres in the IRES, but not in the BS, where collagen bundles lost their clear outlines and inter-bundle spaces, and appeared congealed together, forming a ground substance (Figure 3h vs. m). The collagen fibre density and orientation were similar between IRES, BS and CS (Figures 3q and S6). In IRES, the elastin fibres appeared fragmented and clumped especially around the appendages (Figures 3i and S1b); however, their orientation was not different from the orientation of elastin fibres in the normal skin (Figure 3 d). In BS, the elastin fibres were clumped and fragmented in the lower part of the dermis, different from the normal elastin fibres that have a random orientation (CS; Figures 3n and S1d). Additional ECM proteins (laminin, collagen IV and nephronectin) appeared intact in IRES, but scattered or not visible in BS (Figures 3j,o and S4). Using PS-OCT, birefringence and DOP, we showed that the IRES values were not different from CS immediately after injury, but were significantly different compared with BS (decreased by 72% and increased by 55% for birefringence and DOP, respectively; Figure 3g,l,p). This is consistent with previous reports where using PS-OCT (Park *et al.*, 2001) found that in BS collagen is denatured and loses its birefringence, explaining both the reduction in birefringence and the increase in DOP.

In contrast to burn injury that completely destroyed skin architecture, IRE preserved the skin microarchitecture and affected mostly the cell membranes. One week after injury, in striking contrast to BS, IRES still showed an almost completely preserved stratum corneum, preservation of a majority of the basement membrane and the intercalated structure of the collagen in most parts of the skin (Figures 2d, and S5). The preservation of the ECM in IRES resulted in a strikingly different pattern of inflammatory cells

Table 1. The morphological changes during skin remodelling

Ratio to baseline	IRE_t0	burn_t0	IRE_1w	burn_1w	IRE_3w	burn_3w	IRE_2m	burn_2m	IRE_6m	burn_6m
Whole skin thickness (mm)	**0.73 ± 0.06**	0.99 ± 0.09	0.93 ± 0.09	0.79 ± 0.08	0.96 ± 0.09	**1.35 ± 0.18**	1.14 ± 0.11	**1.27 ± 0.13**	1.02 ± 0.11	1.03 ± 0.10
Stratum corneum thickness (μm)	1.05 ± 0.17	**0.00**	0.51 ± 0.09	**0.00**	**1.99 ± 0.33**	**2.18 ± 0.42**	1.28 ± 0.27	1.70 ± 0.25	1.53 ± 0.35	**2.23 ± 0.43**
Epidermis thickness (μm)	**0.00**	**0.00**	**0.00**	**0.00**	**3.49 ± 0.48**	**5.37 ± 0.72**	1.48 ± 0.24	**3.85 ± 0.23**	0.98 ± 0.25	**2.59 ± 0.35**
Dermis thickness	0.82 ± 0.08	1.06 ± 0.11	1.09 ± 0.13	0.84 ± 0.09	1.07 ± 0.12	1.14 ± 0.11	1.10 ± 0.11	1.30 ± 0.24	0.77 ± 0.28	0.63 ± 0.22
Number of viable hair follicles (per 2 mm)	1.01 ± 0.14	**0.00**	**0.00**	**0.00**	**0.27 ± 0.05**	**0.00**	**0.00**	**0.01 ± 0.01**	**1.35 ± 0.28**	**0.00**
Number of viable sebaceous glands (per 2 mm)	1.05 ± 0.13	**0.00**	**0.00**	**0.00**	**0.00**	**0.00**	0.72 ± 0.20	**0.00**	0.99 ± 1.19	**0.00**
Number of arrector pili (per 2 mm)	0.99 ± 0.11	**0.00**	**0.00**	**0.00**	**0.00**	**0.00**	**0.38 ± 0.20**	**0.00**	0.92 ± 0.19	**0.00**
Number of fibroblasts (150 × 500 micron)	1.03 ± 0.09	**0.69 ± 0.09**	**0.53 ± 0.09**	**0.43 ± 0.09**	**4.68 ± 0.52**	**8.27 ± 0.75**	1.36 ± 0.30	**4.97 ± 1.15**	0.92 ± 0.13	**2.43 ± 0.22**
Number of mast cells (20 × Toloiden blue)	0.71 ± 0.07	**0.34 ± 0.07**	**0.11 ± 0.07**	**0.00**	**2.19 ± 0.24**	**2.00 ± 0.33**	0.83 ± 0.11	1.24 ± 0.23	0.82 ± 0.09	**0.29 ± 0.06**
Number of nerves	0.92 ± 0.12	**0.00**	0.77 ± 0.17	**0.00**	0.90 ± 0.15	1.03 ± 0.16	0.77 ± 0.14	0.51 ± 0.14	**1.83 ± 0.34**	1.15 ± 0.19
Fat layer thickness (μm)	0.52 ± 0.14	1.56 ± 0.45	1.61 ± 0.47	1.28 ± 0.47	**0.00**	**0.03 ± 0.03**	0.87 ± 0.27	0.44 ± 0.45	1.48 ± 0.49	1.00 ± 0.36
Muscle layer thickness (μm)	**0.51 ± 0.07**	0.89 ± 0.09	0.56 ± 0.19	**0.38 ± 0.08**	0.68 ± 0.06	1.36 ± 0.22	1.12 ± 0.18	0.75 ± 0.15	0.96 ± 0.09	0.83 ± 0.23

Ratio to the control skin is shown. In bold, significant changes between the treated skin compared with control skin ($P < 0.05$). Statistical analysis was first done with one-way ANOVA and then with Dunnett's test for treated vs. control skin at all time points. ± SD is shown.

IRE, irreversible electroporation.

migration and sequestration compared with BS as described above. BS did not show this type of demarcation, and there was infiltration of neutrophils throughout the entire affected skin at both 24 h and 1 week after the injury (Figures 6c,e, and S5e). The polarization properties measured with PS-OCT at 1 week revealed a gradual decrease of birefringence for IRES by −33% as compared with CS, and an increase of 25% for the DOP compared with CS (Figure 6a,d,l,m). This finding indicates either a decreased integrity of the collagen fibres, or secretion of new uncrosslinked collagen, thereby reducing the birefringence and depolarizing power. PS-OCT at 1 week after BS revealed no significant change compared with the values immediately after injury, with a birefringence reduced by 57% and a DOP increased by 51% compared with CS (Figure 2a,e,l,m). One week after injuries, the BS formed a extensive scab, which fell off about 11 days after the injury (Figures 2e, and S5e–h). In contrast, IRES did not form a significant scab, but instead displayed partial sloughing of the superficial layers of the skin 10–14 days after ablation.

We further investigated the wound-healing processes at up to 6 months following injury. Three weeks after injury, IRES exhibited multiple foci of normal collagen with normal fibre bundle architecture separated from other foci that appeared to be connected to one another by tracks of cells that were associated with an eightfold increase in fibroblasts (Figure 4a,b,d). We also observed substantial deposition of newly formed uncrosslinked collagen (Figure 4b) associated with the appearance of multiple small blood vessels in the area (Figure 4c). Unlike BS injury, which did not show regeneration of skin appendages, 3 weeks after the injury the epidermis of IRES displayed some bulging of epidermal cells (Figures 4d, arrow, and S7–S9), forming small plug-like areas associated with invaginations of small basoloid cells that form very discrete nests (Figure 4a, arrows). In other areas, there was a proliferation of basaloid cells spreading down from the epidermis forming structures that resembled hair papilla. In some fields, the basaloid proliferation was directly correlated with granularity of the epidermis similar to a follicular orifice (Figure 4a). The forming follicles showed increased expression of folliculogenesis and hair growth regulation markers including laminin (Li *et al.*, 2003a; Tamiolakis *et al.*, 2001), collagen IV (Tamiolakis *et al.*, 2001), nephronectin (Toyoshima *et al.*, 2012), p63 (Ehama *et al.*, 2007), ker17 (Ito *et al.*, 2007), FGF-5 (Hébert *et al.*, 1994), Lef-1 (Ito *et al.*, 2007), BMP-4 (Millar, 2002) and nestin (Li *et al.*, 2003b) 3 weeks after the injury (Figures 4, and S7–S9). These results show faster hair growth in IRES than the previous work of Ito *et al.* (2007) who observed "epidermal downgrowths that resembled developing embryonic hair follicles" 14–19 days after the excisional wound (Ito *et al.*, 2007). This rapid regeneration process can be related to the preservation of ECM following IRES similar to what has been described in the excisional wound-healing model.

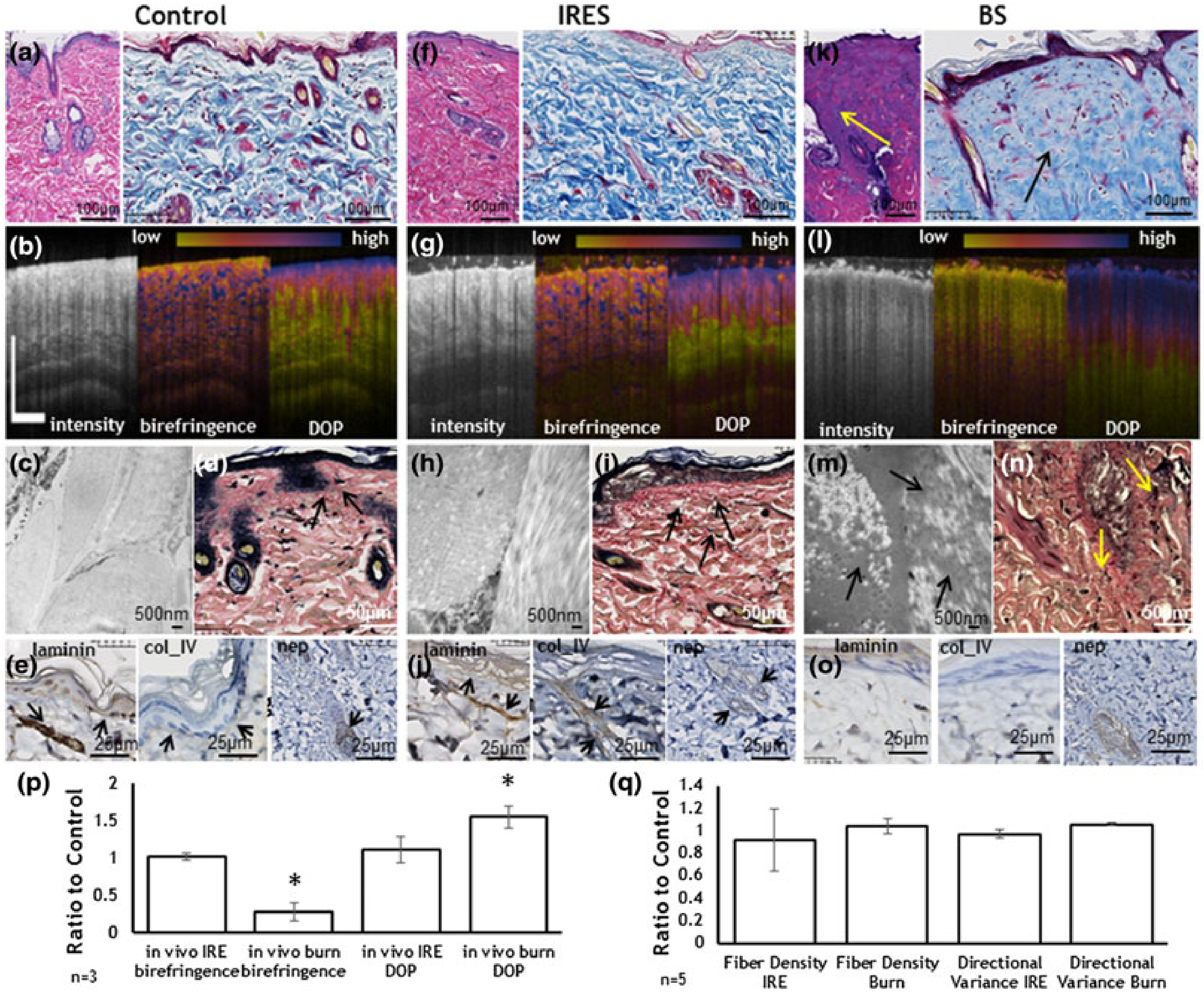

Figure 3. Immediate effects of irreversible electroporation (IRE) and burn injuries on extracellular matrix (ECM). (a) Normal skin pathology [H&E (left), Masson's trichrome (right)]. (b) Polarization-sensitive optical coherence tomography (PS-OCT) imaging of normal rat skin [intensity (left), birefringence (centre), degree of polarization (DOP) (right)]. (c) Transmission electron microscopy image of dermis in normal skin. (d) Verhoeff–Van Gieson stain for collagen in normal skin. Black arrows show normal elastin fibres. (e) Immunohistological staining for ECM structural proteins in normal skin [laminin (left), collagen IV (centre) and nephronectin (right)]. No structural changes were observed in the skin immediately after IRE (f–j). (f) IRE-ablated skin (IRES) pathology (same as a). (g) PS-OCT imaging of IRE skin (same as b). (h) Transmission electron microscopy image of dermis in IRES. (i) Verhoeff–Van Gieson stain for collagen in IRES. Black arrows show elastin fibres. (j) Immunohistological staining for ECM structural proteins in IRES (same as e). Burn caused a significant alteration in the organization of the ECM fibres. (k) Burn skin pathology (same as a). Arrows show an area of melted dermis. (l) PS-OCT imaging of the burn skin (same as b). (m) Transmission electron microscopy image of dermis in burn skin. Arrows show the destroyed collagen fibres. (n) Verhoeff–Van Gieson stain for collagen in burn skin. Arrows show destructed elastin fibres. (o) Immunohistological staining for ECM structural proteins in IRES (same as e). (p) Birefringence and DOP, measured *in vivo* with PS-OCT, of IRE and burned skin in comparison to non-treated control skin. (q) Changes in fibre density and orientation variance after the IRE and burn injury as detected by the computational analysis of the histological slides (Figure S2). Star indicates significant difference compared with control skin ($P < 0.05$). Five animals were used per group for histology ($n = 5$). Three rats were used for the PS-OCT ($n = 3$) [Colour figure can be viewed at wileyonlinelibrary.com]

Two months after the injury, IRES showed remarkable remodelling of skin with its appendages; however, the epidermis was still significantly ($P < 0.05$) thicker than the CS, indicating that the remodelling process was persistent (Figure 5a–d). IRES completely restored its visual appearance 6 months after the injury (Figure 5e–h). The only difference between IRES and CS was the higher melanin level in IRES, giving the skin a tanner hue. Restoration of the polarization properties was observed in IRES by longitudinal *in vivo* imaging using PS-OCT (Figures 5f, and 6l,m). Despite the differences in the initial response to injury, we detected similar polarization properties in both IRES and BS evident by low birefringence, paired with a high DOP, characteristic of the small, freshly synthesized thin collagen fibres and macroscopically homogenous appearance (Figure 6f,g, l–o). Subsequently, the maturing collagen fibres caused an increase in birefringence, observed in both IRES and BS (Figure 6h–l). The dense alignment of the collagen fibres in the burn scars (Figures 6n and S6) only marginally disturbed the polarization state of the probing light, achieving a high DOP throughout the entire 6-month period of this study (Figures 5f and 6i,k,m–o). In contrast, the haphazard organization of the collagen and the appearance of skin appendages in the regenerating IRES resulted in a marked decrease of the DOP with time, achieving values comparable to CS 6 months after injury (Figures 5f–h and 6h,j,m–o).

The total thickness of IRES injury was not different from the thickness of the normal, untreated skin starting

DOI: 10.1002/term

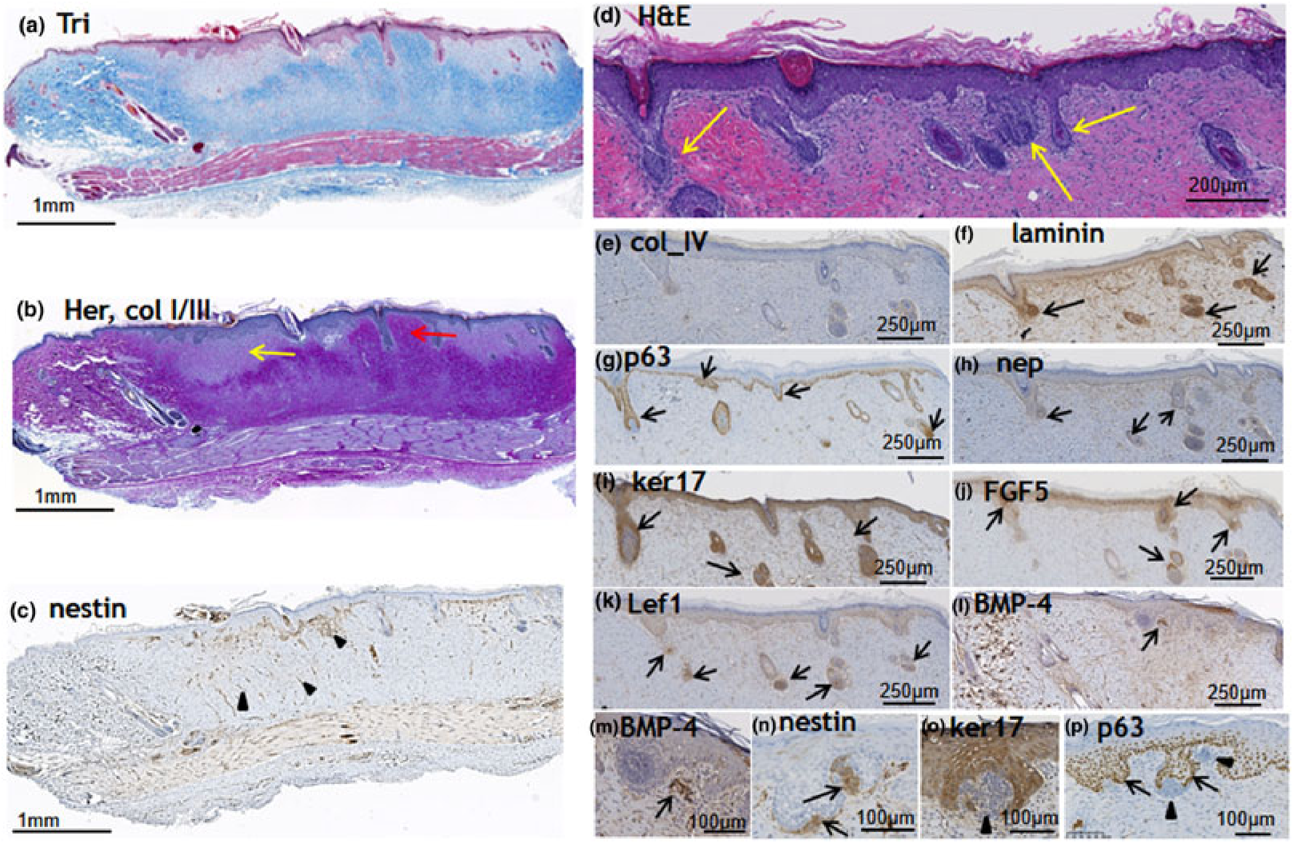

Figure 4. Skin regeneration 3 weeks after irreversible electroporation (IRE). (a) Extracellular matrix (ECM) structure (Masson's trichrome stain). (b) The area is rich with fresh type III collagen (blue in the shown Herovichi staining). The yellow arrow indicates the areas with new uncrosslinked collagen. The red arrow shows the formation of a new hair in the middle of the ablated zone. (c) Angiogenesis, detected with nestin staining. Reduced formation of new vessels in comparison with 3 days and 1 week time points. Hair folliculogenesis at the IRE-ablated site 3 weeks after the injury (d–p). (d) Pathology of the site reveals the formation of new hair follicles at multiple locations inside the injured area (H&E staining). The arrows show the newly formed follicles. (e) Increased expression of collagen IV in the basement membrane. (f) Increased expression of laminin in the basement membrane. (e) Increased expression of nephronectin in the basement membrane. (g, p) Increased expression of p63 in the external part of the forming hair follicles, absence in the hair papilla (arrowheads). (i, o) Increased expression of ker17 in the external part of the forming hair follicles, absence in the hair papilla (arrow heads). (j) Increased expression of FGF-5 in the hair bulging area. (k) Increased expression of Lef-1 in the hair papilla. (l) Increased expression of BMP-4 in the hair papilla area. (n) Increased expression of nestin in the hair papilla area. Combined, the expression of the markers displayed in (d–p) demonstrates the generation of new hair follicles at the ablated site. Five animals were used for this time point [Colour figure can be viewed at wileyonlinelibrary.com]

from 3 weeks after the injury ($P = 0.3$). The BS, however, showed a 35% increase in the skin thickness 3 weeks after the injury, and did not recover to the normal thickness until 6 months after the initial burn (Table 1). Both IRES and BS showed a hyperkeratosis with a doubling of the stratum corneum 3 weeks after the injury, resolving at 6 months for IRES ($P = 0.09$ with CS), but not resolving in the BS. A threefold thickening of the epidermis in the IRES and fivefold thickening in the BS were observed 3 weeks after the injury, which resulted in a near doubling of Young's modulus in the BS skin (Figure 6p). Notably, the epidermal thickness of IRES was only twofold larger than CS 2 months after the injury and completely restored to the original thickness at the 6 month time point ($P = 0.45$); however, the BS epidermal thickness remained 2.5-fold thicker than CS even 6 months after the injury.

After 2 months of remodelling, the collagen in the IRES became thicker than in CS, the fibres were more dense, multifocal and exhibited a pattern resembling normal reticular dermis (Figures 5 and 6h,n,o), resulting in the gradual increase of birefringence and reduction of DOP as observed with PS-OCT (Figures 5 and 6l,m). Six months after injury, IRES exhibited many intercalated fibres with normal skin structure; however, the interfascicular spaces were reduced in comparison with CS (Figures 5 and 6j,n,o). The number of fibroblasts was not different between IRES and CS ($P = 0.28$; Table 1). In contrast to IRES, BS showed an obvious scar without any intercalated collagen fibres 6 months after the injury (Figures 6k,n,o and S1). The number of fibroblasts in BS was 2.5-fold higher than in CS even 6 months after the injury (Table 1).

Hair folliculogenesis resulted in the formation of mature hair, sebaceous glands and arrector pili muscle 2 months after the injury, with restoration of the original number of hairs and other skin appendages 6 months after the injury (Table 1; $P = 0.1$). The hairs in IRES (2 and 6 months after the injury), in contrast to CS, featured follicle complexes consisting of three–four individual hairs (Figure S10). Interestingly, BS at 2 and 6 months likewise showed a few attempts of folliculogenesis, evident by a single bulging of the epidermis; this, however, did not progress to the formation of the hair papilla, presumably due to the extensive collagen deposition in the underlying tissue, inhibiting the hair development.

In both IRES and BS, panniculus carnosus completely reformed 2 months after the injury (Figures 5 and 6h,i;

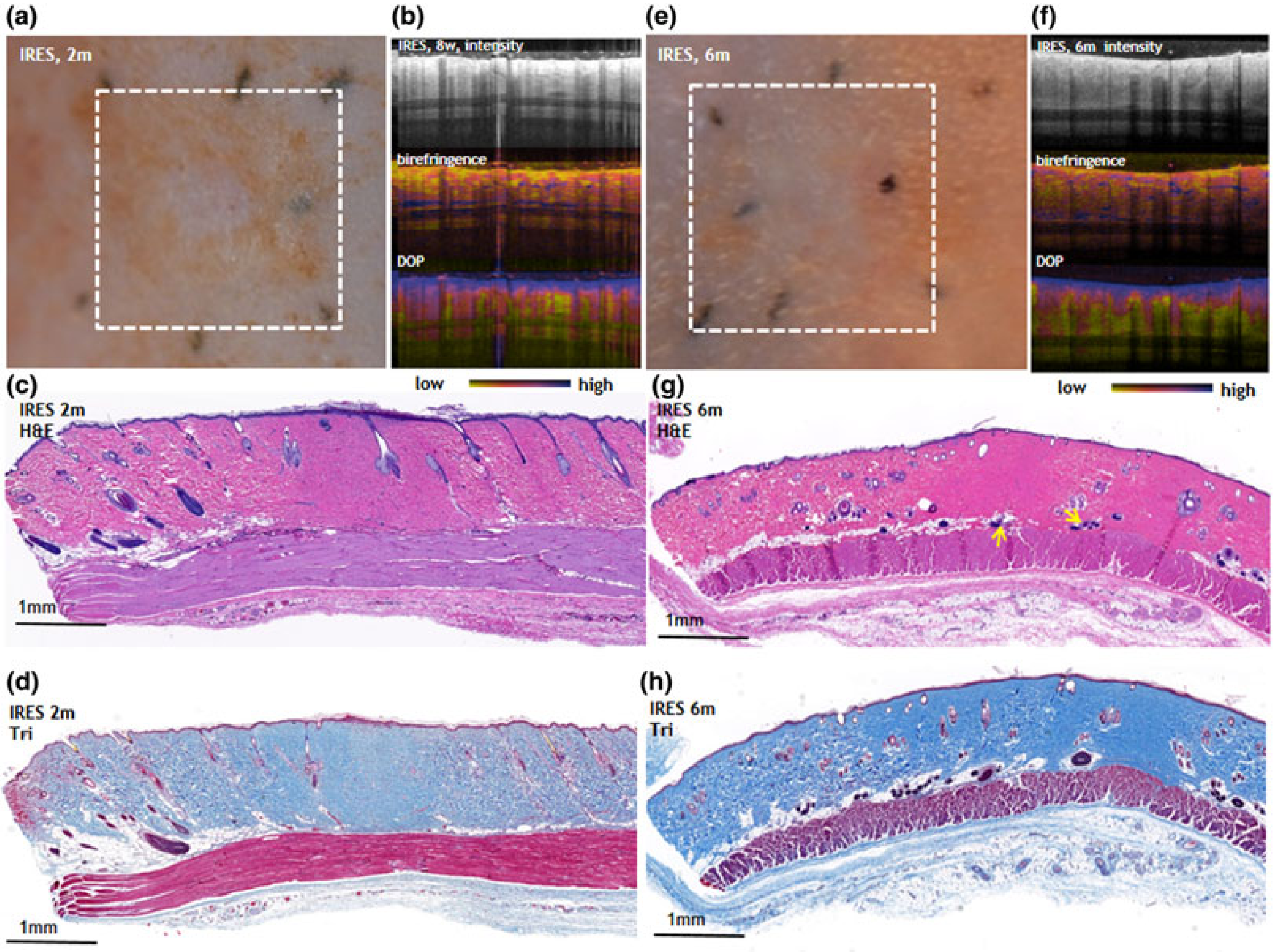

Figure 5. Late, remodelling phase, events in the irreversible electroporation (IRES). (a) Digital image (2 months after IRE). (b) Polarization-sensitive optical coherence tomography (PS-OCT) 2 months after IRE. (c) Histology 2 months after IRE (H&E stain). (d) Histology 2 months after IRE (Masson's trichrome stain). (e) Digital image (6 months after IRE). (f) PS-OCT 6 months after IRE. (g) Histology 6 months after IRE (H&E stain), yellow arrows show regenerating hair follicles. (h) Histology 6 months after IRE (Masson's trichrome stain) [Colour figure can be viewed at wileyonlinelibrary.com]

Table 1). Six months after the injury, the muscle fibres, however, showed hypertrophy and a loss of intermuscular spaces (Figures 5 and 6j,k). The striation of the muscle fibres appeared normal with only some single cells still exhibiting loss of striation. Most of the nuclei were present in the site-centre of the fibres. Vasculature in both IRES and BS showed a marked dilation in multiple vessels 3 weeks after the injury (Figures 5 and 6f,g,q). The vasculature in the dermis of IRES resembled that of CS 6 months after the injury (Figures 5 and 6j,q). In contrast, 6 months following the injury, the vasculature of BS exhibited larger vessels, oriented perpendicular to the axis of the epidermis (Figure 6k,q).

In addition to histological evaluation and *in vivo* PS-OCT imaging, we compared the protein levels of selected cytokine and growth factors, which are known to mediate tissue degeneration and remodelling using multiplex technology. We analysed skin protein extracts from samples obtained from rats subjected to IRES and BS at 6 h, and at 2 and 5 weeks after the injury (Table 2). We found that 6 h after the injury, IRES showed higher expression of MCP-1 and TNF-α protein levels compared with BS ($P < 0.002$). Two weeks after injury following scab sloughing off the skin, the IRES showed a significantly lower expression of MCP-1 and MIP-1α than BS ($P < 0.002$), while both levels were higher than in CS. Importantly, previous studies in humans with alopecia areata have found increased expression levels of MCP-1, and proposed to prevent the overexpression of this chemokine for alopecia treatment (Benoit *et al.*, 2003). Our study provides additional clues on the importance of MCP-1 in promoting skin appendage development as its increased level was associated with scar formation and absence of folliculogenesis at the late phase of BS skin remodelling in contrast to IRES injury (Tables 1 and 2). Previous animal studies have shown that the decreased levels of MIP-1α lead to less collagen synthesis in murine wounds (DiPietro *et al.*, 1998). Our results show that BS expresses significantly higher levels of MIP-1α compared with IRES that regenerates without scars (Table 2). The levels of the MIP-1α in the IRES are still higher than its levels in the CS, and are associated with the normal wound-healing process.

The hypothesis that preserved ECM enhances tissue healing was described decades ago (Yannas *et al.*, 1989), and there are many studies suggesting that introducing ECM-based scaffolds can improve healing and result in better regeneration results (Berthiaume *et al.*, 2011).

DOI: 10.1002/term

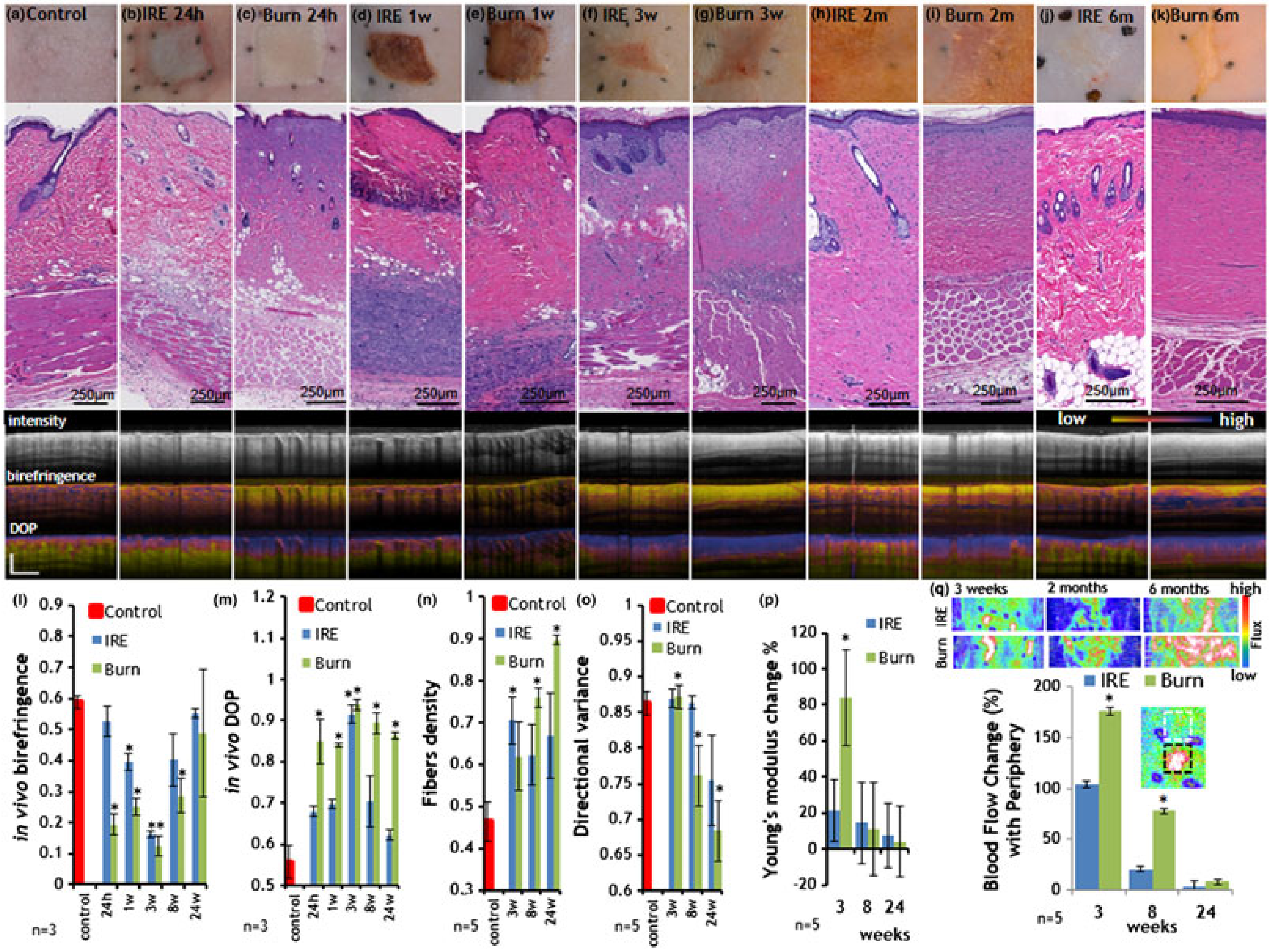

Figure 6. Dynamics of skin wound healing after irreversible electroporation (IRE) and burn injury. For images (a–k), three panels are shown. The top panel shows the digital photograph of the wound site at the indicated time point. The medium panel shows the H&E stain of that region. The bottom panel shows the *in vivo* polarizarion-sensitive optical coherence tomography (PS-OCT) images as follows: top: intensity centre: birefringence; bottom: degree of polarization (DOP). (a) Control, normal skin. (b) IRE skin 24 h after the injury. (c) Burn skin 24 h after the injury. (d) IRE skin 1 week after the injury. (e) Burn skin 1 week after the injury. (f) IRE skin 3 weeks after the injury. (g) Burn skin 3 weeks after the injury. (h) IRE skin 2 months after the injury. (i) Burn skin 2 months after the injury. (j) IRE skin 6 months after the injury. (k) Burn skin 6 months after the injury. (l) Birefringence as calculated from *in vivo* PS-OCT. (m) DOP as calculated from the *in vivo* PS-OCT signal. (n) Fibre density quantified from digitized histopathology slides. (o) Directional variance of the fibre orientation as calculated from histopathology slides. (p) Young's modulus of the injured skin compared with control skin. (q) Change in blood flow rate at the centre of the wound in comparison with the flux at the periphery. The top panel shows the images as reconstructed from the Doppler imaging. The plot shows the ratio of the flow in the lesion centre, and the adjacent, not affected area. The insert shows an example of regions of interests from which the flux ratio was calculated. The star indicates significant difference compared with control skin ($P < 0.05$). For control values in images (l–o), the average values from 10 animals were used. For experimental groups, five animals were used. For PS-OCT images, three rats were imaged [Colour figure can be viewed at wileyonlinelibrary.com]

However, none of these studies could provide an *in vivo* evidence of the importance of naïve ECM organization. Many investigators over the last decade showed that fetal wounds demonstrate scarless healing (Coolen *et al.*, 2010); however, fetal wounds are different from the adult tissues in their chemical composition, lack of inflammatory response and ECM structure. To study tissue regeneration *in vivo*, several animal models have been used including amphibians (Song *et al.*, 2011), rabbits (Ramos *et al.*, 2008), pigs (Ramos *et al.*, 2008) and mice (Ito *et al.*, 2007). *De novo* skin appendages regeneration in the wound area has been reported during the last 60 years in mice (Ito *et al.*, 2007), rats (Mikhail, 1963), rabbits (Billingham and Russell, 1956; Breedis, 1954) and humans (Beachkofsky *et al.*, 2011; Kligman and Strauss, 1956). Even though the importance of the 3D environment in the restoration of dermal papilla inductivity has been recently demonstrated (Higgins *et al.*, 2013), none of the existing *in vivo* models could explore the effects of the natural ECM on scar formation and skin appendage regeneration due to the lack of *in vivo* decellularization methods. The IRE injury model used in this study provides a viable *in vivo* tool to study the tissue regeneration following cellular ablation in the setting for preserved ECM. This model provides an opportunity to study the effect of naïve structure on wound healing. The major limitation of this study was the chosen animal species as the rodent skin structure and wound healing is different from that of human skin. Yet, the ability to eliminate the cells in the area without damaging ECM structure is important for basic research projects aimed at studying skin cellular development, structure formation, scarring and interactions of stem cells with their niches, and have traditionally been performed in rodent models (Hsu *et al.*, 2014; Seifert *et al.*, 2012).

Our study provides detailed information on the dynamics of wound healing after IRE. These dynamics

Table 2. The immunological response of rat skin tissue to burn and IRE injury

	IRE_6h	IRE_2w	IRE_5w	burn_6h	burn_2w	burn_5w
G-CSF (13)	1.38 ± 0.66	1.40 ± 0.78	1.07 ± 0.58	0.31 ± 0.28	1.51 ± 0.76	1.36 ± 0.70
Eotaxin (14)	1.00 ± 0.31	1.15 ± 0.33	1.28 ± 0.57	0.72 ± 0.21	1.22 ± 0.33	0.80 ± 0.30
IL-1a (19)	0.27 ± 0.25	0.98 ± 0.82	1.61 ± 1.27	0.08 ± 0. 08	0.64 ± 0.49	1.19 ± 0.98
Leptin (22)	1.31 ± 0.83	0.65 ± 0.47	1.54 ± 1.06	1.02 ± 0.90	0.90 ± 0.55	0.64 ± 0.40
MIP-1a (33)	11.35 ± 6.94	19.10 ± 9.29	1.38 ± 0.32	1.97 ± 0.51	127.73 ± 12.74	6.28 ± 6.14
IL-4 (34)	1.48 ± 0.48	1.76 ± 0.56	1.97 ± 0.90	1.20 ± 0.49	2.74 ± 0.71	1.26 ± 0.42
IL-1b (35)	7.99 ± 5.86	4.03 ± 2.10	2.70 ± 1.39	2.59 ± 1.12	14.27 ± 4.50	1.82 ± 0.76
IL-2 (36)	1.12 ± 0.47	1.45 ± 0.62	1.16 ± 0.54	0.40 ± 0.41	1.33 ± 0.53	0.74 ± 0.45
IL-6 (37)	10.80 ± 7.35	1.62 ± 1.03	0.78 ± 0.29	2.58 ± 1.87	3.71 ± 0.86	0.58 ± 0.24
EGF (38)	3.22 ± 2.97	0.49 ± 0.28	0.84 ± 0.46	1.31 ± 0.98	4.18 ± 1.98	1.25 ± 1.28
IL-13 (39)	0.63 ± 0.28	1.15 ± 0.52	1.23 ± 0.65	0.41 ± 0.29	1.35 ± 0.44	0.41 ± 0.59
IL-10 (51)	2.14 ± 0.25	2.55 ± 0.79	1.19 ± 0.39	0.96 ± 0.43	3.68 ± 0.35	0.96 ± 0.17
IL-12p70 (52)	1.03 ± 0.77	1.51 ± 0.91	1.40 ± 0.93	0.85 ± 0.68	2.21 ± 1.30	1.01 ± 0.65
IFNy (53)	1.23 ± 0.12	1.32 ± 0.12	1.37 ± 0.23	0.80 ± 0.19	1.39 ± 0.11	0.99 ± 0.27
IL-18 (57)	0.38 ± 0.35	2.25 ± 1.59	1.58 ± 1.20	0.08 ± 0.06	3.06 ± 2.16	1.09 ± 0.80
MCP-1 (62)	7.08 ± 3.92	2.29 ± 1.27	1.78 ± 1.12	1.14 ± 0.77	6.21 ± 3.39	1.50 ± 1.10
IP-10 (65)	2.35 ± 1.16	31.85 ± 18.22	2.82 ± 2.26	1.40 ± 0.88	21.45 ± 10.02	10.43 ± 9.35
VEGF (73)	1.79 ± 1.26	3.07 ± 1.99	1.19 ± 0.93	1.23 ± 0.87	10.61 ± 6.85	0.88 ± 0.57
Fractalkine (74)	0.78 ± 0.55	0.90 ± 0.24	1.25 ± 0.36	0.31 ± 0.08	0.79 ± 0.17	0.67 ± 0.19
LIX (75)	3.41 ± 1.92	1.90 ± 0.80	0.94 ± 0.40	1.19 ± 0.58	16.35 ± 5.41	1.09 ± 0.59
MIP-2 (76)	28.29 ± 23.56	77.33 ± 31.18	1.24 ± 0.76	3.33 ± 0.68	449.37 ± 5.11	1.65 ± 0.88
TNFa (77)	1.36 ± 0.46	3.10 ± 1.16	1.54 ± 0.95	0.64 ± 0.22	18.31 ± 6.01	1.76 ± 0.96
RANTES (78)	0.89 ± 0.82	8.75 ± 7.74	2.71 ± 2.51	0.84 ± 0.84	3.79 ± 3.22	5.71 ± 5.23
TGF-B1 (18)	2.07 ± 1.09	2.39 ± 0.83	0.99 ± 0.38	3.11 ± 1.37	3.04 ± 1.05	1.36 ± 0.65
TGF-B2 (54)	0.62 ± 0.30	2.58 ± 1.14	1.27 ± 0.47	0.77 ± 0.21	2.62 ± 0.63	1.40 ± 0.86
TGF-B3 (36)	0.50 ± 0.17	3.17 ± 0.85	1.02 ± 0.38	0.70 ± 0.12	2.14 ± 0.34	1.38 ± 0.98

Ratio to control, untreated skin is shown. Marked in red/green are cytokine expression levels that are significantly higher/lower ($P < 0.002$) in one group as compared with the other group at the matching time point (marked in green). ± SD is shown.
IRE, irreversible electroporation.

are important for treatment monitoring. Our findings provide a new direction for research on wound healing and tissue scarless regeneration, using pulsed electric fields as a method to achieve decellularization (Sano *et al.*, 2010). Such *in vivo* decellularization could be used for basic studies on cell migration patterns and differentiation at various skin compartments, information useful for skin development, wound healing and cancer research. Furthermore, this could help in elucidating the mechanisms of skin regeneration by providing an acellular injury micro-environment. In addition, this acellular environment could be used in the future for cell transplantations studies and therapies, providing new treatments for skin abnormalities for patients. In addition, our data suggest that the preservation of the architecture of the ECM in IRES and the reduction in levels of MCP-1 and MIP-1α, as compared with burns, promote scarless healing and the formation of hair follicles, sebaceous glands, panniculus carnosus and arrector pili muscle. In contrast, the damage caused by burn injury provokes increased fibrosis and ultimately leads to the formation of a scar. In addition to the mechanistic insight of the role played by the ECM in tissue regeneration, it would be necessary to unravel the molecular signalling enabled by the preservation of the ECM. Future work will address how the orientation and structure of the ECM is guiding attachment patterns of signalling molecules, cell migration, differentiation and morphogenesis. Additional studies to elucidate the role of immune cells infiltration in the regenerating IRES in comparison to the infiltration in the non-regenerating BS, and study the source of cells that contribute to appendages formation are warranted. We believe that our model of scarless healing in mammals using IRE ablation will provide a missing key-element for regeneration of entire organs and the study of morphogenesis. This model can be used in further studies in combination with specific cell type depletion to understand the role of specific cells during skin. Furthermore, it can be used for cell transplantation or cell lineages tracking studies (Driskell *et al.*, 2013) to understand the sources of appendage regeneration. Finally, pulsed electric field ablation may provide a new method to study and modulate the stem cell niche (Lane *et al.*, 2014), a critical element in tissue regeneration.

Conflict of interest

The authors declare no conflict of interest.

Acknowledgments

The authors acknowledge Shriners Grant #85120-BOS and Bionational USA-Israel Science Foundation (BSF) for the support of this study BSF Grant # 2015286. Research in this publication was also supported in part by the Department of Defense, Air Force Office of Scientific Research under agreement number FA9550-13-1-0068, and the National Institute of Biomedical Imaging and Bioengineering of the National Institutes of Health, award P41 EB015903. Electron microscopy was performed in the Microscopy Core of the Center for Systems Biology/Program in Membrane Biology, which is partially supported by an Inflammatory Bowel Disease Grant DK43351 and a Boston Area Diabetes and Endocrinology Research Center (BADERC) Award DK57521. The authors thank Dana-Farber/Harvard Cancer Center in Boston, MA, for the use of the Rodent Histopathology Core, which provided histopathology service. Dana-Farber/

Harvard Cancer Center is supported in part by NCI Cancer Center Support Grant # NIH 5 P30 CA06516.

Competing financial interests

The authors declare no competing financial interests.

Author contribution statement

AG, MB, MCM, MY: conceived study; AG, MV, FB, HA, SK: did the experiments; AG, MV, MW, KQ IG, WA, MB, BB, MCM, MY: analysed the data; AG, MV, HA MCM, MY: wrote the paper.

References

Aarabi S, Bhatt KA, Shi Y *et al*. 2007; Mechanical load initiates hypertrophic scar formation through decreased cellular apoptosis. *FASEB J* **21**: 3250–3261.

Beachkofsky TM, Henning JS, Hivnor CM. 2011; Induction of de novo hair regeneration in scars after fractionated carbon dioxide laser therapy in three patients. *Dermatol Surg* **37**: 1365–1368. http://www.ncbi.nlm.nih.gov/pubmed/21492302.

Benoit S, Toksoy A, Goebeler M, Gillitzer R. 2003; Selective expression of chemokine monokine induced by interferon-gamma in alopecia areata. *J Invest Dermatol* **121**: 933–935. doi:https://doi.org/10.1046/j.1523-1747.2003.12524.x.

Berthiaume F, Maguire TJ, Yarmush ML. 2011; Tissue engineering and regenerative medicine: history, progress, and challenges. *Annu Rev Chem Biomol Eng* **2**: 403–430. http://www.annualreviews.org/doi/abs/10.1146/annurev-chembioeng-061010-114257.

Billingham R, Russell P. 1956; Incomplete wound contracture and the phenomenon of hair neogenesis in rabbits' skin. *Nature* **177**: 791–792. http://www.ncbi.nlm.nih.gov/pubmed/13321965.

Breedis C. 1954; Regeneration of hair follicles and sebaceous glands from the epithelium of scars in the rabbit. *Cancer Res* **14**: 575–579. http://www.ncbi.nlm.nih.gov/pubmed/13199800.

Chunlan J, Davalos RV, Bischof JC. 2015; A review of basic to clinical studies of irreversible electroporation therapy. *Biomed Eng IEEE Trans* **62**: 4–20.

Coolen NA, Schouten KCWM, Boekema BKHL, Middelkoop E, Ulrich MMW. 2010; Wound healing in a fetal, adult, and scar tissue model: a comparative study. *Wound Repair Regen* **18**: 291–301.

Crowley JM. 1973; Electrical breakdown of bimolecular lipid membranes as an electromechanical instability. *Biophys J* **13**: 711–724.

Cruzeiro-Hansson L, Mouritsen OG. 1988; Passive ion permeability of lipid membranes modelled via lipid-domain interfacial area. *BBA – Biomembr* **944**: 63–72.

Deodhar A, Dickfeld T, Single GW *et al*. 2011; Irreversible electroporation near the heart: ventricular arrhythmias can be prevented with ECG synchronization. *Am J Roentgenol* **196**: W330–W335.

DiPietro LA. 2013; Angiogenesis and scar formation in healing wounds. *Curr Opin Rheumatol* **25**: 87–91.

DiPietro LA, Burdick M, Low QE, Kunkel SL, Strieter RM. 1998; MIP-1alpha as a critical macrophage chemoattractant in murine wound repair. *J Clin Invest* **101**: 1693–1698. http://www.pubmedcentral.nih.gov/articlerender.fcgi?artid=508751&tool=pmcentrez&rendertype=abstract.

Driskell RR, Lichtenberger BM, Hoste E *et al*. 2013; Distinct fibroblast lineages determine dermal architecture in skin development and repair. *Nature* **504**: 277–281. http://www.nature.com/nature/journal/v504/n7479/full/nature12783.html?WT.ec_id=NATURE-20131212.

Duffield JS, Lupher M, Thannickal VJ, Wynn TA. 2013; Host responses in tissue repair and fibrosis. *Annu Rev Pathol Mech Dis* **8**: 241–276.

Ehama R, Ishimatsu-Tsuji Y, Iriyama S *et al*. 2007; Hair follicle regeneration using grafted rodent and human cells. *J Invest Dermatol* **127**: 2106–2115. doi:https://doi.org/10.1038/sj.jid.5700823.

Eto H, Suga H, Aoi N *et al*. 2012; Therapeutic potential of fibroblast growth factor-2 for hypertrophic scars: upregulation of MMP-1 and HGF expression. *Lab Investig* **92**: 214–223. https://doi.org/10.1038/labinvest.2011.127.

Gibran N. 2014; The genetics and epigenetics of extreme healing: hypertrophic scars and diabetic ulcers (337.4). *FASEB J* **28**: 337.4. http://www.fasebj.org/content/28/1_Supplement/337.4.

Golberg A, Bruinsma BG, Jaramillo M, Yarmush M, Uygun BE. 2016a; Rat liver regeneration following ablation with irreversible electroporation. *PeerJ* **4**: e1571.

Golberg A, Bruinsma BG, Uygun BE, Yarmush ML. 2015a; Tissue heterogeneity in structure and conductivity contribute to cell survival during irreversible electroporation ablation by "electric field sinks". *Sci Rep* **5**: 8485. http://www.nature.com/srep/2015/150216/srep08485/full/srep08485.html.

Golberg A, Khan S, Belov V *et al*. 2015b; Skin rejuvenation with non-invasive pulsed electric fields. *Sci Rep* **5**: 10 187. http://www.nature.com/srep/2015/150512/srep10187/full/srep10187.html.

Golberg A, Villiger M, Khan S *et al*. 2016b; Preventing scars after injury with partial irreversible electroporation. *J Invest Dermatol* **136**: 2297–2304.

Golberg A, Yarmush ML. 2013; Nonthermal irreversible electroporation: fundamentals, applications, and challenges. *IEEE Trans Biomed Eng* **60**: 707–714.

Hasgall, PA, Neufeld E, Gosselin M, Klingenböck A, Kuster N. 2014; IT'IS Database for thermal and electromagnetic parameters of biological tissues, Version 2.5, August 1st, 2014. www.itis.ethz.ch/database.

Hébert JM, Rosenquist T, Götz J, Martin GR. 1994; FGF5 as a regulator of the hair growth cycle: evidence from targeted and spontaneous mutations. *Cell* **78**: 1017–1025. http://www.ncbi.nlm.nih.gov/pubmed/7923352.

Higgins CA, Chen JC, Cerise JE, Jahoda CAB, Christiano AM. 2013; Microenvironmental reprogramming by three-dimensional culture enables dermal papilla cells to induce de novo human hair-follicle growth. *Proc Natl Acad Sci U S A* **110**: 19 679–19 688. http://www.pnas.org/content/110/49/19679.abstract.

Hsu Y-C, Li L, Fuchs E. 2014; Emerging interactions between skin stem cells and their niches. *Nat Med* **20**: 847–856.

Ito M, Yang Z, Andl T *et al*. 2007; Wnt-dependent de novo hair follicle regeneration in adult mouse skin after wounding. *Nature* **447**: 316–320.

Ivorra A, Al-Sakere B, Rubinsky B, Mir LM. 2009; In vivo electrical conductivity measurements during and after tumor electroporation: conductivity changes reflect the treatment outcome. *Phys Med Biol* **54**: 5949–5963.

Kligman A, Strauss J. 1956; The formation of vellus hair follicles from human adult epidermis. *J Invest Dermatol* **27**: 19–23. http://www.ncbi.nlm.nih.gov/pubmed/13357817.

Koh TJ, DiPietro LA. 2011; Inflammation and wound healing: the role of the macrophage. *Expert Rev Mol Med* **13**: e23.

Kotnik T, Kramar P, Pucihar G, Miklavčič D, Tarek M. 2012; Cell membrane electroporation – Part 1: the phenomenon. *IEEE Electr Insul Mag* **28**: 14–23.

Lane SW, Williams DA, Watt FM. 2014; Modulating the stem cell niche for tissue regeneration. *Nat Biotechnol* **32**: 795–803. https://doi.org/10.1038/nbt.2978.

Lee EW, Thai S, Kee ST. 2010; Irreversible electroporation: a novel image-guided cancer therapy. *Gut Liver* **4** (Suppl 1): S99–S104.

Li J, Tzu J, Chen Y *et al*. 2003a; Laminin-10 is crucial for hair morphogenesis. *EMBO J* **22**: 2400–2410. http://www.pubmedcentral.nih.gov/articlerender.fcgi?artid=155997&tool=pmcentrez&rendertype=abstract.

Li L, Mignone J, Yang M *et al*. 2003b; Nestin expression in hair follicle sheath progenitor cells. *Proc Natl Acad Sci U S A* **100**: 9958–9961. http://www.pubmedcentral.nih.gov/articlerender.fcgi?artid=187900&tool=pmcentrez&rendertype=abstract.

Lo WCY, Villiger M, Golberg A *et al*. 2016; Longitudinal, 3D in vivo imaging of collagen remodeling in murine hypertrophic scars using polarization-sensitive optical frequency domain imaging. *J Invest Dermatol* **136**: 84–92. http://www.ncbi.nlm.nih.gov/pubmed/26447821.

Matsuda Y, Hagio M, Ishiwata T. 2013; Nestin: a novel angiogenesis marker and possible target for tumor angiogenesis. *World J Gastroenterol* **19**: 42–48.

Michael D, O'Neill M. 1970; Electrohydrodynamic instability in plane layers of fluid. *J Fluid Mech* **41**: 571–580.

Mikhail GR. 1963; Hair neogenesis in rat skin. *Arch Dermatol* **88**: 713. http://archderm.jamanetwork.com/article.aspx?articleid=528310.

Millar SE. 2002; Molecular mechanisms regulating hair follicle development. *J Invest Dermatol* **118**: 216–225.

Narayanan G. 2011; Irreversible electroporation for treatment of liver cancer. *Gastroenterol Hepatol (NY)* **7**: 313–316. http://www.pubmedcentral.nih.gov/articlerender.fcgi?artid=3127037&tool=pmcentrez&rendertype=abstract.

Park BH, Saxer C, Srinivas SM, Nelson JS, de Boer JF. 2001; In vivo burn depth determination by high-speed fiber-based polarization sensitive optical coherence tomography. *J Biomed Opt* **6**: 474–479.

Pavšelj N, Miklavčič D. 2008; A numerical model of permeabilized skin with local transport regions. *IEEE Trans Biomed Eng* **55**: 1927–1930.

Philips P, Hays D, Martin RCG. 2013; Irreversible electroporation ablation (IRE) of unresectable soft tissue tumors: learning curve evaluation in the first 150 patients treated. *PLoS One* **8**: e76260. http://journals.plos.org/plosone/article?id=10.1371/journal.pone.0076260.

Phillips M, Maor E, Rubinsky B. 2010; Nonthermal irreversible electroporation for tissue decellularization. *J Biomech Eng* **132**: 091003. http://biomechanical.asmedigitalcollection.asme.org/article.aspx?articleID=1426746.

Phillips MA, Narayan R, Padath T, Rubinsky B. 2012; Irreversible electroporation on the small intestine. *Br J Cancer* **106**: 490–495.

Place ES, Evans ND, Stevens MM. 2009; Complexity in biomaterials for tissue engineering. *Nat Mater* **8**: 457–470.

Quinn KP, Golberg A, Broelsch GF *et al*. 2015; An automated image processing method to quantify collagen fibre organization within cutaneous scar tissue. *Exp Dermatol* **24**: 78–80. http://www.ncbi.nlm.nih.gov/pubmed/25256009.

Ramos MLC, Gragnani A, Ferreira LM. 2008; Is there an ideal animal model to study hypertrophic scarring? *J Burn Care Res* **29**: 363–368. http://www.ncbi.nlm.nih.gov/pubmed/18354295.

Robson MC. 2003; Proliferative scarring. *Surg Clin North Am* **83**: 557–569.

Rubinsky B. 2007; Irreversible electroporation in medicine. *Technol Cancer Res Treat* **6**: 255–260.

Rubinsky B, Onik G, Mikus P. 2007; Irreversible electroporation: a new ablation modality – clinical implications. *Technol Cancer Res Treat* **6**: 37–48.

Russell SB, Russell JD, Trupin KM *et al*. 2010; Epigenetically altered wound healing in keloid fibroblasts. *J Invest Dermatol* **130**: 2489–2496. http://www.pubmedcentral.nih.gov/articlerender.fcgi?artid=2939920&tool=pmcentrez&rendertype=abstract.

Sano MB, Neal RE, Garcia PA, Gerber D, Robertson J, Davalos RV. 2010; Towards the creation of decellularized organ constructs using irreversible electroporation and active mechanical perfusion. *Biomed Eng Online* **9**: 83. http://www.biomedical-engineering-online.com/content/9/1/83.

Seifert AW, Kiama SG, Seifert MG, Goheen JR, Palmer TM, Maden M. 2012; Skin shedding and tissue regeneration in African spiny mice (Acomys). *Nature*

489: 561–565. http://www.nature.com.ezp-prod1.hul.harvard.edu/nature/journal/v489/n7417/full/nature11499.html.

Smith JC, Boone BE, Opalenik SR, Williams SM, Russell SB. 2008; Gene profiling of keloid fibroblasts shows altered expression in multiple fibrosis-associated pathways. *J Invest Dermatol* **128**: 1298–1310. http://www.pubmedcentral.nih.gov/articlerender.fcgi?artid=2933038&tool=pmcentrez&rendertype=abstract.

Song F, Li B, Stocum DL. 2011; Amphibians as research models for regenerative medicine. *Organ* **6**: 141–150.

Sonnemann KJ, Bement WM. 2011; Wound repair: toward understanding and integration of single-cell and multicellular wound responses. *Annu Rev Cell Dev Biol* **27**: 237–263.

Spugnini EP, Arancia G, Porrello A *et al*. 2007; Ultrastructural modifications of cell membranes induced by “electroporation” on melanoma xenografts. *Microsc Res Tech* **70**: 1041–1050.

Steinchen A, Gallez D, Sanfeld A. 1982; A viscoelastic approach to the hydrodynamic stability of membranes. *J Colloid Interface Sci* **85**: 5–15.

Sugár I. 1979; A theory of the electric field-induced phase transition of phospholipid bilayers. *Biochim Biophys Acta* **556**: 72–85.

Tamiolakis D, Papadopoulos N, Anastasiadis P *et al*. 2001; Expression of laminin, type IV collagen and fibronectin molecules is related to embryonal skin and epidermal appendage morphogenesis. *Clin Exp Obstet Gynecol* **28**: 179–182. http://www.ncbi.nlm.nih.gov/pubmed/11530869.

Thompson CM, Hocking AM, Honari S, Muffley LA, Ga M, Gibran NS. 2013; Genetic risk factors for hypertrophic scar development. *J Burn Care Res* **34**: 477–482. http://www.pubmedcentral.nih.gov/articlerender.fcgi?artid=3786175&tool=pmcentrez&rendertype=abstract.

Toyoshima K, Asakawa K, Ishibashi N *et al*. 2012; Fully functional hair follicle regeneration through the rearrangement of stem cells and their niches. *Nat Commun* **3**: 784. http://www.nature.com/ncomms/journal/v3/n4/full/ncomms1784.html?WT.ec_i..

Tsong TY. 1991; Electroporation of cell membranes. *Biophys J* **60**: 297–306.

Villiger M, Zhang EZ, Nadkarni SK, Oh WY, Vakoc BJ, Bouma BE. 2013; Spectral binning for mitigation of polarization mode dispersion artifacts in catheter-based optical frequency domain imaging. *Opt Express* **21**: 16353–16369. http://ovidsp.ovid.com/ovidweb.cgi?T=JS&CSC=Y&NEWS=N&PAGE=fulltext&D=medl&AN=23938487\nhttp://sfx.bibl.ulaval.ca:9003/sfx_local?sid=OVID:medline&id=pmid:23938487&id=doi:10.1364/OE.21.016353&issn=1094-4087&isbn=&volume=21&issue=14&spage=16353&pages=16353-6.

Weaver JC. 2000; Electroporation of cells and tissues. *IEEE Trans Plasma Sci* **28**: 24–33.

Weaver JC, Chizmadzhev YA. 1996; Theory of electroporation: a review. *Bioelectrochem Bioenerg* **41**: 135–160. http://www.sciencedirect.com/science/article/pii/S0302459896050623.

Wong VW, Rustad KC, Akaishi S *et al*. 2011; Focal adhesion kinase links mechanical force to skin fibrosis via inflammatory signaling. *Nat Med* **18**: 148–152.

Yannas IV, Lee E, Orgill DP, Skrabut EM, Murphy GF. 1989; Synthesis and characterization of a model extracellular matrix that induces partial regeneration of adult mammalian skin. *Proc Natl Acad Sci U S A* **86**: 933–937. http://www.pubmedcentral.nih.gov/articlerender.fcgi?artid=286593&tool=pmcentrez&rendertype=abstract.

Yarmush ML, Golberg A, Serša G, Kotnik T, Miklavčič D. 2014; Electroporation-based technologies for medicine: principles, applications, and challenges. *Annu Rev Biomed Eng* **16**: 295–320. http://www.annualreviews.org/doi/abs/10.1146/annurev-bioeng-071813-104622?journalCode=bioeng.

Supporting information

Additional Supporting Information may be found online in the supporting information tab for this article.

Figure S1. Immediate effects of burn and IRE on the rat skin. a. H&E staining IRES. b. Verhoeff–Van Gieson stain for collagen in IRE ablated skin. Arrows show elastin fibers. c. H&E burn injury. d. Verhoeff–Van Gieson stain for collagen in IRE ablated skin. Arrows show elastin fibers

Figure S2. Cell apoptosis following IRE. Tissue harvested at post IRE a. immediately; b. 6 hours; c. 12 hours; d. 24 hours; e. 3 days; f. 1 week. Red color shows normal cells, green/orange color shows apoptotic cells

Figure S3. The effects of IRE on the normal rat skin 6 hours after ablation

Figure S4. The effects of IRE and thermal injury on specific extracellular matrix fibers. Effects on a. laminin, b. collagen IV and c. nephronectin are shown

Figure S5. The effects of IRE and third degree burn 1 week after the injury. a. IRES overview 1 week after injury (H&S). Arrows show the line, made by neutrophils, which separated the areas into section with degraded and normal ECM. Lower arrow show the nerve without axons but which preserved its structure. Insert shows the decellularised large blood vessel. An arrow shows decellularized vessel wall. b. Preserved stratum corneum in the IRES. c. Mitotic, double nuclear panniculus carnosus cells (arrows). d. Preserved structure of a nerve in the IRES. Axons are missing. e. BS overview 1 week after injury (H&E). f. Destroyed stratum corneum of the BS. g. Necrotic fibers of panniculus carnosus (arrow). h. Destroyed structure of nerves in the BS

Figure S6. Fiber density and directional variance from the control, IRE and burn skin at different time points, from the immediate up to 24 weeks after injury. Top panel: Masson’s Trichrome stain. Wound regions were manually selected within a 0.3 x 0.7 mm window delineating the wound center, wound edge and an adjacent, uninjured region. Central panel: automated colorimetric analysis of each pixel enabled the identification of collagen-containing pixels, and collagen fibers density measurements were significantly higher within the scar. Bottom panel: pixel-wise analysis of the fiber direction enabled quantification of the local fiber alignment, and its directional variance. It was significantly lower within the burn scar than in the control skin or IRE skin twenty-four weeks after the injury. No differences were found between control and IRE skin at eight weeks and twenty-four weeks. Five animals were analyzed for each time point

Figure S7. Expression of a. BMP4, b. collagen IV and c. keratin 17 in the hair follicles of normal (control) and IRES three weeks after the complete ablation

Figure S8. Expression of a. Lef1, b. nephronectin and c. nestin in the hair follicles of normal (control) and IRES three weeks after the complete ablation

Figure S9. Expression of a. p63, b. laminin and c. FGF5 in the hair follicles of normal (control) and IRES three weeks after the complete ablation

Figure S10. Regenerated hair in the IRES. Quadrupled hair are shown with an arrow

Table S1 Electrical properties used for Finite Element modeling of electric field distribution in the skin